EDGE ARTICLE

Check for updates

Impact of the d^0 transition metal on local structural transformations in disordered rock salt cathodes

Tianyu Li, [ab] Otavio Marques,[c] Tullio S. Geraci,[de] Erick A. Lawrence, [ab] Arava Zohar,[ab] Jue Liu, [f] Evans Avoka,[dg] Alexandra Navrotsky,[deg] Johanna Nelson Weker [c] and Raphaële J. Clément [*ab]

Although it is widely accepted that the long-range (average) crystal structure plays a critical role in determining the electrochemical performance of battery materials, the relationship between local structural features and electrochemical performance is rarely studied. Disordered rock salt oxides (DRX), which have become serious contenders for next generation Li-ion electrode materials, provide an ideal platform for exploring correlations between local structure and electrochemical performance as they exhibit a simple face-centered cubic structure and combine long-range disorder and short-range order on the cation sublattice. This work examines the $Li_{1.1}Mn_{0.7}Zr_{0.2-x}Ti_xO_2$ series of DRX cathodes and investigates the links between local structure rearrangements and capacity activation. The end-member $Li_{1.1}Mn_{0.7}Zr_{0.2}O_2$ compound exhibits a low capacity in the as-synthesized state, attributed to unfavorable short-range order that hinders Li-ion transport, yet its capacity increases seven-fold, from 20 to 140 mAh g^{-1}, after chemical delithiation followed by a 400 °C heat treatment. Capacity activation is associated with the appearance of local spinel-like structural features that depart from the short-range order originally present in the material, without significant change to the bulk composition and average crystal structure. Investigation of a series of $Li_{1.1}Mn_{0.7}Zr_{0.2-x}Ti_xO_2$ ($x \leq 0.2$) DRX compounds reveals that the correlation length of the spinel-like ordering that emerges during the heat treatment strongly depends on the Zr : Ti ratio. Yet, dramatic capacity activation and electrochemical (pseudo-)plateaus reminiscent of Mn-based spinel cathodes are observed for all compounds irrespective of the size of the ordered domains. To explain this phenomenon, we propose that the DRX phase undergoes a complete transformation to a spinel-like domain structure, which improves bulk Li-ion transport regardless of domain size.

Introduction

In secondary batteries, the positive (cathode) and negative (anode) electrodes are responsible for energy storage and play a key role in device performance. For intercalation-type electrodes used in commercial Li- and Na-ion cells, the bulk composition and average crystal structure have a direct impact

[a]Materials Department, University of California Santa Barbara, Santa Barbara, CA 93106, USA. E-mail: rclement@ucsb.edu

[b]Materials Research Laboratory, University of California Santa Barbara, Santa Barbara, CA 93106, USA

[c]Stanford Synchrotron Radiation Lightsource, SLAC National Accelerator Laboratory, Menlo Park, California 94025, USA

[d]Navrotsky Eyring Center for Materials of the Universe, Arizona State University, Tempe, AZ 85287, USA

[e]School of Molecular Sciences, Arizona State University, Tempe, AZ 85287, USA

[f]Neutron Scattering Division, Oak Ridge National Laboratory, Oak Ridge, Tennessee 37831, USA

[g]Ira A. Fulton School for Engineering of Matter, Transport and Energy, Arizona State University, Tempe, AZ 85287, USA

on the electrochemical properties,[1,2] including the average potential,[3–6] cycling stability,[7–9] and ionic[10–12] and electronic[11,13,14] conductivity. For example, in layered NMC ($LiNi_x$-$Mn_yCo_{1-x-y}O_2$) cathodes, Li-ion transport occurs within the two dimensional Li slabs and electron transport occurs within the transition metal (TM) slabs and is supported by a 90° O–TM–O bonding network.[15] The layered structure stabilized by the combination of redox-active Ni and Co species, and inactive Mn^{4+}, leads to reasonably fast long-range charge transport, which explains why NMCs remain most widely used despite intensive research efforts into Ni- and Co-free cathode chemistries. While the links between the long-range crystal structure and performance are well understood for many electrode systems, comparatively little attention has been paid to local structural features, with most of the work in this area focused on anti-site defects,[16–20] stacking faults[21–25] and the distribution of dopants or substituents on the TM sublattice.[26–29]

Disordered rock salt oxides/oxyfluorides (DRX) have emerged as promising Li-ion electrode materials, with recent studies demonstrating that DRX cathodes[30–32] and anodes[33–35] based on

sustainable and cost-effective chemistries could supplant state-of-the-art NMC cathodes[1,36,37] and the $Li_4Ti_5O_{12}$ anode.[38-41] As their name suggests, DRX compounds, with general formula $Li_yTM_{2-y}O_{2-z}F_z$ (typically, $1 \leq y \leq 1.4$, $z \leq 0.67$), adopt a simple face-centered cubic (fcc) NaCl-type structure, where Li and TM species share the cation site and O species occupy the anion site. Yet, this description fails to capture short-range correlations between cations and anions, which have been found to significantly impact the electrochemical behavior.[30,31,42-44]

Previous studies have shown that Li-ion transport in DRX electrodes proceeds through octahedral–tetrahedral–octahedral (O–T–O) pathways, where the migration energy barrier depends on the number of TM that face-share with the intermediate tetrahedral site.[42,45] In particular, long-range Li-ion transport requires the formation of a percolating network of low barrier diffusion channels—typically 0-TM channels, where the tetrahedral sites share faces only with Li-filled or vacant octahedra—and their connection through a limited number of 1-TM channels.[46] In the fully disordered (random) limit, the distribution of 0-TM, 1-TM, 2-TM, 3-TM and 4-TM channels is determined by the cation ratio, with Li excess strongly enhancing 0-TM percolation.

Short-range order in pristine DRX cathodes has been found to reduce the fraction of 0-TM channels relative to the random limit. This ordering has been associated with the presence of hypervalent (d^0) TM species (e.g., Ti^{4+}, Zr^{4+} or Nb^{5+})[30-32,42,47-50] and/or with partial substitution of O^{2-} by F^- anions,[51-53] both of which are introduced to compensate for Li excess and stabilize the structure. Notably, the Li : TM ratio and F content in Li_y-$TM_{2-y}O_{2-z}F_z$ compositions influence not only local cation ordering but also the nature of the redox processes, both of which govern the electrochemical performance[54-56] and are often challenging to disentangle.

Achieving precise control over short-range order without altering the overall DRX composition remains a major challenge. Ceder and coworkers[50] demonstrated in $Li_{1.2}Mn_{0.55}$-$Ti_{0.25}O_{1.85}F_{0.15}$ that employing a rapid temperature ramp during calcination followed by fast quenching to room temperature suppresses short-range order compared to slow heating and cooling, leading to a moderate increase in capacity from 273 to 313 mAh g^{-1}. In this work, we show that, in $Li_{1.1}Mn_{0.7}Zr_{0.2-x}$-$Ti_xO_2$ ($0 \leq x \leq 0.2$), local cation ordering can be manipulated through a chemical and heat treatment, resulting in significant capacity enhancements. The Zr : Ti ratio further controls the size of the structural domains that emerge during treatment.

Focusing first on the $Li_{1.1}Mn_{0.7}Zr_{0.2}O_2$ end-member, we find that chemical delithiation followed by a 400 °C heat treatment results in a seven-fold capacity enhancement (from ~20 mAh g^{-1} to ~140 mAh g^{-1}) without changing the overall cathode composition and average structure. Using synchrotron X-ray and neutron diffraction, pair distribution function (PDF) analysis, X-ray absorption and solid-state nuclear magnetic resonance (NMR) spectroscopy, we show that the remarkable capacity enhancement is associated with the formation of nanoscale spinel-like cation ordered domains (less than 20 Å in size). This represents the first successful attempt to significantly

improve the electrochemical performance of a DRX cathode by tuning the local structure without altering its composition and long-range structure. We contrast the evolution of the $Li_{1.1}$-$Mn_{0.7}Zr_{0.2}O_2$ cathode to that of $Li_{1.1}Mn_{0.7}Ti_{0.2}O_2$ following a similar chemical delithiation and heat treatment process and show that, while both Mn and Ti species tend to cluster to form spinel domains in the latter compound, Zr species become more isolated from other TM species in the former compound. The impact of composition on the local structural rearrangements is further investigated for a series of $Li_{1.1}Mn_{0.7}Zr_{0.2-x}$-$Ti_xO_2$ DRX cathodes. We find that, as the Zr : Ti ratio decreases, the correlation length of the spinel-like short-range order that emerges during the heat treatment gradually increases. Regardless of the size of the ordered domains that emerge after transformation, significant capacity enhancements are observed across the entire DRX series. However, the final capacity achieved after transformation decreases with the correlation length of the ordered domains. We propose that the spinel domains are separated by antiphase boundaries, as has been shown previously,[57] and that Li-ion transport is impeded by the higher density of these planar defects in the Zr-rich compositions. Overall, our findings indicate that the d^0 TM species plays a key role in controlling the DRX-to-spinel local structural transformation, and that the nature of cation short-range order and lengthscale of the ordered domains are at least as important as the average crystal structure in determining the electrochemical properties.

Results

Structure and electrochemical performance of as-synthesized $Li_{1.1}Mn_{0.7}Zr_{0.2}O_2$

The $Li_{1.1}Mn_{0.7}Zr_{0.2}O_2$ DRX compound was obtained by heating a stoichiometric and ball-milled mixture of Li_2CO_3, Mn_2O_3 and ZrO_2 to 1100 °C under Ar gas flow, followed by a rapid quench to room temperature under air. Details of the synthesis procedure are provided in the SI file. The time-of-flight neutron diffraction pattern of as-synthesized $Li_{1.1}Mn_{0.7}Zr_{0.2}O_2$, along with its Rietveld refinement fit, is shown in Fig. 1a. The diffraction data can be fit using the $Fm\bar{3}m$ rock salt structure, where Li, Mn, and Zr are randomly distributed among the octahedral 4a sites, indicating a cation-disordered long-range structure. Examination of the structure at the local scale, however, suggests some deviation from full cation disorder. The neutron pair distribution function (NPDF) data collected over the 1.5–3.5 Å range is shown in Fig. 1b, along with fits using two different structural models. A distinct splitting of the ~2 Å negative peak corresponding to cation (Li, Mn and Zr)-oxygen correlations is observed, which cannot be fit using a fully cation-disordered cubic rock salt model, and instead requires a cation-ordered tetragonal rock salt (γ-$LiFeO_2$-like) model. Hence, at the very local scale, Li and Zr/Mn species occupy distinct octahedral sites in the rock salt structure, as observed for $Li_{1.1}Mn_{0.4}Zr_{0.4}O_2$ by Ceder,[48] Butala[58] and coworkers. Given the high valence of Zr^{4+} and its similar ionic size (0.72 Å) to Li^+ (0.76 Å), we hypothesize that the observed γ-$LiFeO_2$-like short-range correlations arise from minimization of the coulombic repulsion
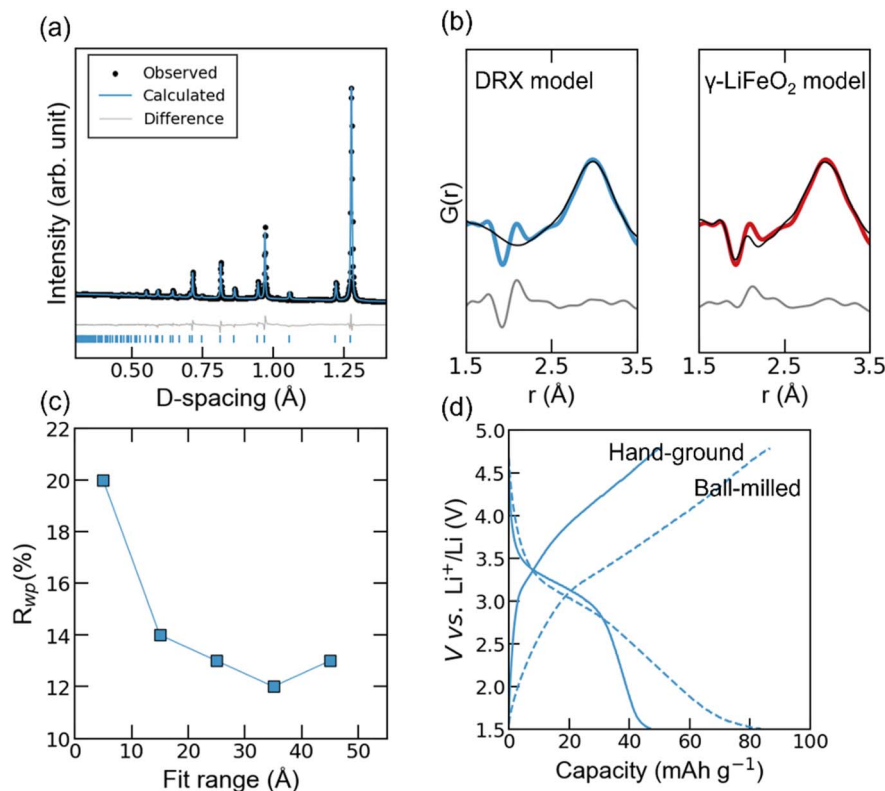
Fig. 1 (a) Neutron diffraction pattern collected on as-synthesized $Li_{1.1}Mn_{0.7}Zr_{0.2}O_2$ with its Rietveld refinement fit. (b) Neutron pair distribution function (PDF) data over the 1.5–3.5 Å range, and small box fits using cation-disordered cubic rock-salt (left panel) and cation-ordered tetragonal (γ-LiFeO$_2$-like) rock-salt (right panel) models. (c) R_{wp} of the small box fits of the neutron PDF data using a cation-disordered cubic rock-salt model over different lengthscales. (d) Second-cycle electrochemical profiles of $Li_{1.1}Mn_{0.7}Zr_{0.2}O_2$ hand ground or ball-milled with carbon during electrode fabrication. The cells were cycled between 1.5 and 4.8 V vs. Li$^+$/Li^0, at a current density of 20 mA g^{-1}.

between Zr^{4+} species, and between Mn^{3+} and Zr^{4+} species. Indeed, the observed cation ordering reduces the occurrence of Zr–Zr, Mn–Mn and Zr–Mn next-nearest-neighbor correlations (and indirectly, Li–Li next-nearest-neighbor correlations), and instead favors Zr–Li and Mn–Li next-nearest-neighbor pairs.[48] Finally, fits of the NPDF data using the cation-disordered cubic rock salt model over different lengthscales are shown in Fig. S1, and the evolution of the corresponding R_{wp} values is plotted in Fig. 1c. As the fitting range increases, the quality of the fit improves, indicating a combination of long-range disorder and short-range correlations in the DRX crystal structure.

Short-range order in $Li_{1.1}Mn_{0.7}Zr_{0.2}O_2$ negatively impacts its electrochemical performance as a Li-ion cathode. The electrochemical profiles of $Li_{1.1}Mn_{0.7}Zr_{0.2}O_2$ cathodes prepared from DRX powders that were either hand ground or ball-milled with carbon (in a 7 : 2 mass ratio of active material:Super C65) during electrode fabrication are shown in Fig. 1d. These profiles were collected during the second charge–discharge cycle between 1.5 and 4.8 V vs. Li$^+$/Li^0 at a rate of 20 mA g^{-1}. As-synthesized $Li_{1.1}Mn_{0.7}Zr_{0.2}O_2$ consists of very large particles (10–50 microns in size), which can be downsized by ball-milling, resulting in particles ranging from hundreds of nanometers to 10 microns, as revealed by the scanning electron microscopy (SEM) images in Fig. S2. Although lower-than-theoretical capacities are typically observed for micron-sized DRX

cathodes,[59–61] the reversible capacity obtained from hand-ground $Li_{1.1}Mn_{0.7}Zr_{0.2}O_2$ is particularly low, at around 45 mAh g^{-1} (solid line in Fig. 1d). After ball-milling with carbon, the capacity of $Li_{1.1}Mn_{0.7}Zr_{0.2}O_2$ almost doubles, reaching 85 mAh g^{-1} (dotted line in Fig. 1d). Nevertheless, this capacity remains well below the theoretical capacity based on the $Mn^{3+/4+}$ redox reservoir (~195 mAh g^{-1}).

As mentioned previously, the presence of clusters of LiO$_6$ octahedra is critical to fast Li-ion transport in DRX compounds.[45] For $Li_{1.1}Mn_{0.7}Zr_{0.2}O_2$, the propensity for Li–Zr and Li–Mn nearest-neighbor correlations significantly reduces the probability of forming these Li-rich clusters. This unfavorable short-range order hinders Li-ion transport and explains its poor capacity, even when the diffusion length of Li-ions in and out of the particles is reduced and the electronic conductivity of the composite is increased by ball-milling with carbon. In contrast, high and near-theoretical initial capacities (≥200 mAh g^{-1}, based on Mn^{3+}/Mn^{4+} redox) have been achieved when ball-milling Ti- and Nb-substituted DRX compounds with a similar Mn content and cycled under similar conditions,[54,56,62,63] suggesting that the d^0 metal plays a central role in the local structure that forms during synthesis. Indeed, Ceder and coworkers[48] have shown that $Li_{1.2}Mn_{0.4}Zr_{0.4}O_2$ exhibits fewer and more isolated Li-rich clusters compared to its Ti analogue, $Li_{1.2}Mn_{0.4}Ti_{0.4}O_2$, severely limiting its capacity and rate capability.

In summary, our structural and electrochemical analysis of the $Li_{1.1}Mn_{0.7}Zr_{0.2}O_2$ cathode indicates the presence of unfavorable short-range order in this compound, which prevents the formation of a percolating network of Li-ion transport channels and severely limits its capacity.

Thermal activation of chemically-delithiated $Li_{0.5}Mn_{0.7}Zr_{0.2}O_2$

$Li_{1.1}Mn_{0.7}Zr_{0.2}O_2$ was chemically delithiated by reacting it with NO_2BF_4 in acetonitrile, following a previously-reported procedure.[64–66] The delithiation reaction proceeds as $Li_{1.1}Mn_{0.7}Zr_{0.2}O_2 + xNO_2BF_4 \rightarrow Li_{1.1-x}Mn_{0.7}Zr_{0.2}O_2 + xNO_2 + LiBF_4$. The amount of Li extracted from the DRX was controlled by tuning the amount of oxidizing agent (NO_2BF_4), the reaction time and the reaction temperature.[55] Approximately half of the Li-ions were removed from the structure, resulting in a composition close to $Li_{0.5}Mn_{0.7}Zr_{0.2}O_2$, as revealed by ICP analysis (Table S1). The resulting $Li_{0.5}Mn_{0.7}Zr_{0.2}O_2$ powder was then subjected to a heat treatment at 400 °C under an inert (Ar) atmosphere. The synchrotron X-ray diffraction (SXRD) patterns obtained on $Li_{0.5}Mn_{0.7}Zr_{0.2}O_2$ before and after the heat treatment are compared in Fig. 2a. Following chemical delithiation, $Li_{0.5}Mn_{0.7}Zr_{0.2}O_2$ retains its cubic DRX structure, as all of the reflections in the diffraction pattern can be indexed using an $Fm\bar{3}m$ model. After the heat treatment, the position, intensity and widths of the reflections remain nearly unchanged,

confirming that the long-range (average) structure of $Li_{0.5}Mn_{0.7}Zr_{0.2}O_2$ is unaltered.

Mn K-edge X-ray absorption near edge structure (XANES) spectra and SEM images collected on $Li_{0.5}Mn_{0.7}Zr_{0.2}O_2$ before and after the heat treatment are shown in Fig. 2b and c. The XANES spectra completely overlap, indicating that the average Mn oxidation state remains the same, and the SEM results reveal no noticeable change in particle morphology or size during the heat treatment process. The absence of significant grain size evolution is consistent with the similar SXRD peak widths observed for $Li_{0.5}Mn_{0.7}Zr_{0.2}O_2$ before and after thermal treatment (Fig. 2a).

We then examined the impact of the heat treatment on the electrochemical performance of $Li_{0.5}Mn_{0.7}Zr_{0.2}O_2$. Second-cycle electrochemical profiles obtained for the chemically delithiated DRX before and after the heat treatment, and hand-ground with carbon, are shown in Fig. 2d. Without heat treatment, the capacity of the chemically delithiated DRX is very low, similar to that of pristine (hand-ground) $Li_{1.1}Mn_{0.7}Zr_{0.2}O_2$ (Fig. 1d). After a 400 °C heat treatment, however, a dramatic, seven-fold increase in capacity is observed, from 20 mAh g^{-1} to 140 mAh g^{-1}. Interestingly, this capacity enhancement cannot be attributed to factors that often underlie variations in electrochemical performance,[67] such as a change in composition, long-range crystal structure, or average particle size, as indicated by
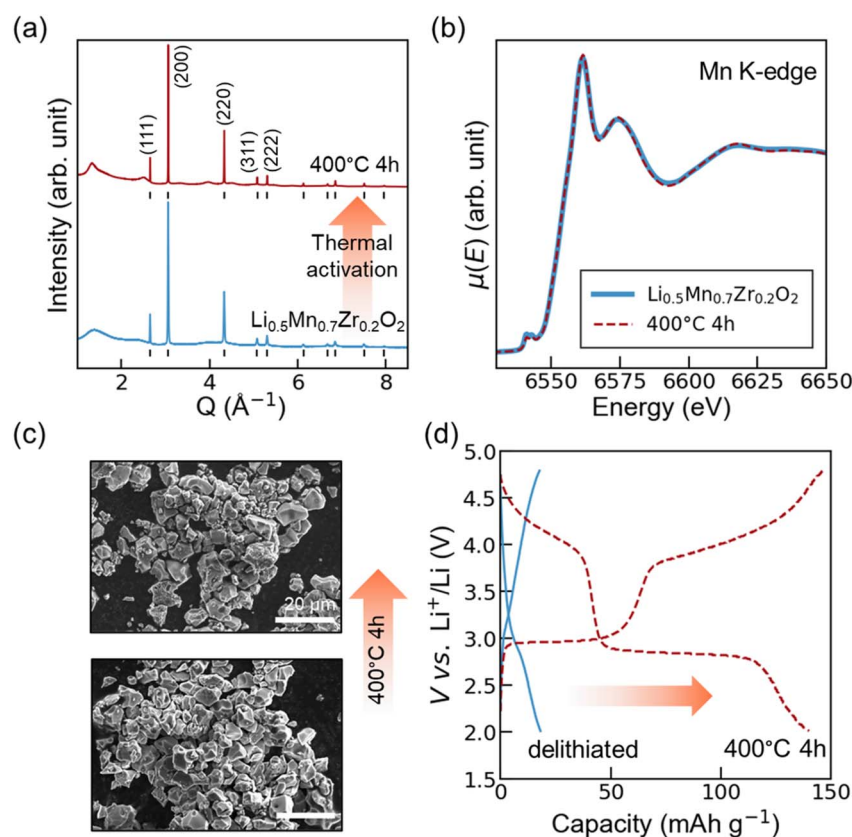

Fig. 2 (a) Synchrotron X-ray diffraction pattern, (b) Mn K-edge XANES, (c) SEM images and (d) second-cycle electrochemical profiles of the $Li_{0.5}Mn_{0.7}Zr_{0.2}O_2$ DRX cathode prepared by chemical delithiation before and after a 400 °C heat treatment for 4 h. The DRX powders were hand ground with carbon during electrode fabrication. The cells were cycled between 1.5 and 4.8 V vs. Li$^+$/Li^0, at a current density of 20 mA g^{-1}.

the present analysis (Fig. 2a–c). In addition to capacity activation, the heat treatment triggers a change in the shape of the electrochemical profile, with the emergence of two (pseudo-) plateaus at 3 V and 4 V vs. Li^+/Li^0. These plateaus are characteristic of $Mn^{3+/4+}$-based spinel cathodes and have been attributed to Li insertion into/deinsertion from octahedral (3 V) and tetrahedral (4 V) sites in the structure.[68,69] Thus, the observation of such plateaus suggests the development of spinel-like short-range order or domains during the heat treatment, even though the long-range rock salt structure is broadly unaltered as noted earlier.

The structural changes identified here can be compared to those observed in "Mn-rich" DRX (i.e., with a Mn content > 0.5) comprising Ti^{4+} or Nb^{5+} as the d^0 metal. Previous reports have indicated that such compounds undergo a phase transformation during electrochemical cycling, resulting in the formation of spinel-like domains evidenced not only by the appearance of electrochemical plateaus at 3 V and 4 V, but also by the emergence of new reflections in the diffraction data. The formation of long-range spinel-like domains within the DRX lattice leads to a structure coined as the "δ phase".[54,55,57] In contrast, the SXRD pattern collected on $Li_{0.5}Mn_{0.7}Zr_{0.2}O_2$ after the heat treatment does not exhibit any new diffraction peaks compared to the pattern obtained before heating (Fig. 2a); instead, very broad (diffuse scattering) peaks emerge on heating to 400 °C, with the more prominent feature at ~1.3 Å. After the heat treatment, the diffuse scattering peaks and sharper DRX reflections can be indexed using a cubic spinel structural model with two hkl-dependent peak widths. hkl with l odd peaks are significantly broader than hkl with l even peaks, which we attribute to the development of coherent short-range spinel domains within the long-range DRX structure, by analogy with our previous work on $Li_yMn_{0.7}Ti_{0.2}O_2$.[55] To support this assignment, we refined the SXRD pattern using a "spinel domain" structural model (Fig. 3, with refined structural parameters listed in Table S3). This model comprises a single cubic spinel phase ($Fd\bar{3}m$ space group, where the 4a octahedral site of the initial DRX structure splits into filled 16c and empty 16d octahedral sites) with hkl l odd and l even reflections fit using different peak widths, and successfully captures the position and peak width of all of the reflections. In contrast, a Rietveld refinement using a single cubic ($Fm\bar{3}m$) DRX phase fails to account for the diffuse scattering, and a refinement using a single cubic spinel $Fd\bar{3}m$ phase with no hkl-dependent peak broadening does not properly capture the width of the peaks (Fig. 3, Tables S4 and S5). From, the "spinel domain" refinement, the average size of the grains and spinel-like domains are estimated to be on the order of 180(2) and 2(1) nm, respectively (the large uncertainty in the size of the domains comes from the extreme broadening of the diffuse scattering peaks). Hence, structural rearrangements take place over 3 and 4 DRX unit cells (~2 spinel unit cells) or over lengthscales <20 Å.

Finally, the "spinel domain" structural model was used to refine the neutron diffraction pattern collected on heat-treated $Li_{0.5}Mn_{0.7}Zr_{0.2}O_2$. Once again, hkl l odd and l even reflections were fit using different peak widths, and the refinement results
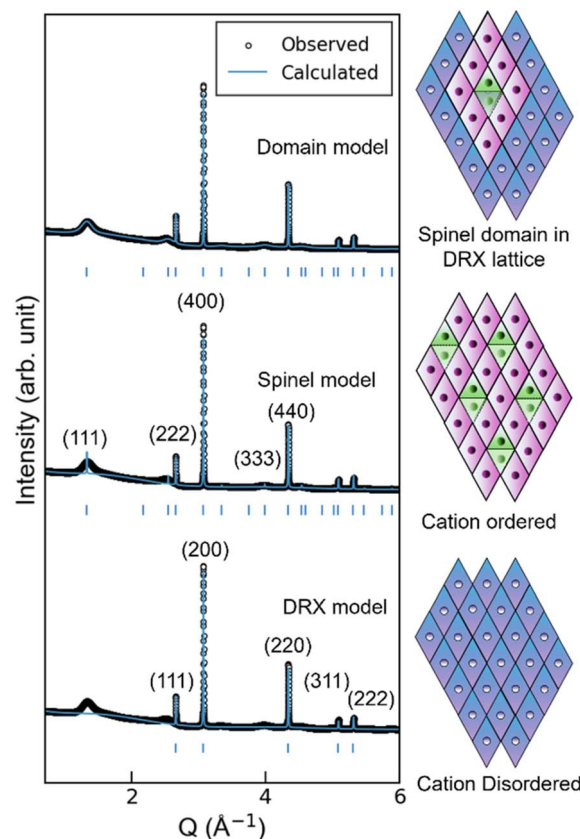

Fig. 3 Rietveld refinements of the synchrotron XRD pattern obtained on the thermally relaxed $Li_{0.5}Mn_{0.7}Zr_{0.2}O_2$ sample using a DRX (bottom), spinel (middle), or spinel domain (top) structural model. The hkl with l odd and l even sets of reflections were fit using two different peak shapes in the third model. The corresponding structural model is depicted on the right of the refinement, where purple represents TM atoms, and green represents Li atoms.

are presented in Fig. S3 and Table S6. The analysis indicates that, in the average structure, 25% of the Li-ions migrate to tetrahedral (8a) sites, with the rest (75%) remaining in (one of the two) octahedral (16c) sites in the spinel structure. By comparison, our previous work showed that nearly all of the Li-ions migrate from octahedral sites to tetrahedral (8a) sites when the chemically delithiated $Li_{0.5}Mn_{0.7}Ti_{0.2}O_2$ DRX undergoes a similar 400 °C heat treatment.[55]

Having established the emergence of spinel domains within the long-range structure of $Li_{0.5}Mn_{0.7}Zr_{0.2}O_2$ using diffraction techniques, we turn to Mn and Zr K-edge X-ray extended absorption fine structure (EXAFS) to investigate the local structure around the TM species following the thermally-induced structural transformation (thermal activation). Fourier-transformed Mn K-edge EXAFS ($\chi(R)$) results on $Li_{0.5}Mn_{0.7}Zr_{0.2}O_2$ before and after the heat treatment are shown in Fig. 4a. The most prominent peaks at ~1.4 Å and ~2.3 Å in the data obtained before thermal activation correspond to nearest-neighbor (Mn–O) and next-nearest-neighbor (Mn–M, with M = Li, Mn, Zr) scattering correlations, respectively. It is important to note that $\chi(R)$ is not a real radial distribution function due to
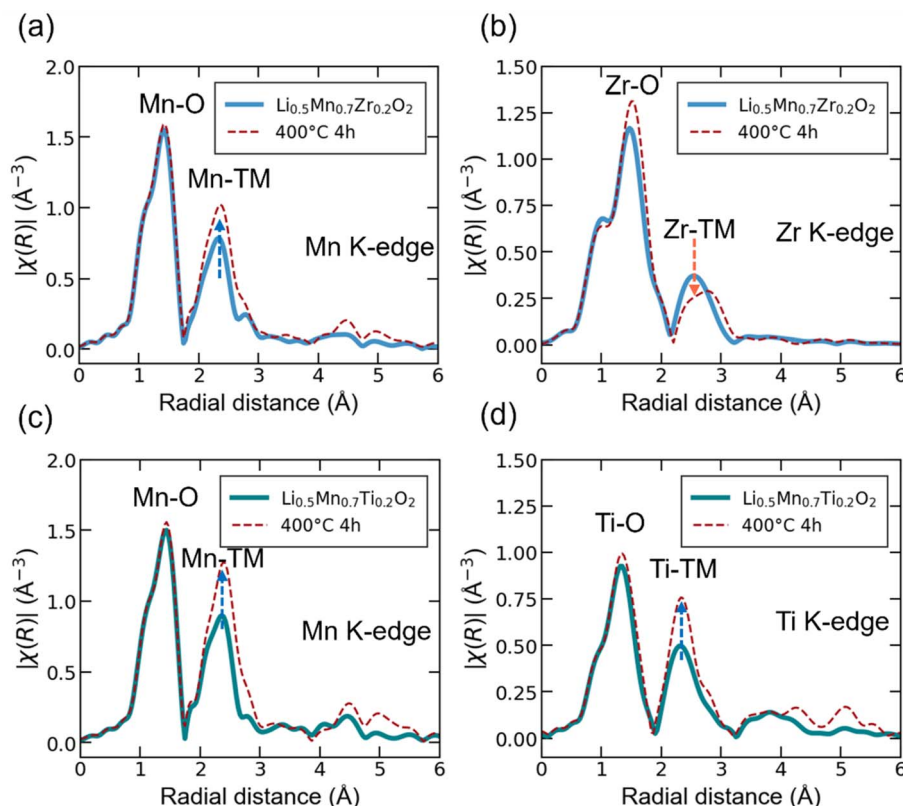
Fig. 4 Fourier-transformed EXAFS ($\chi(R)$) data on chemically delithiated $Li_{0.5}Mn_{0.7}Zr_{0.2}O_2$ ((a), (b)) and $Li_{0.5}Mn_{0.7}Ti_{0.2}O_2$ ((c) and (d)) before and after a 400 °C heat treatment for 4 h. Mn K-edge data are shown in (a) and (c), and data obtained on the d^0 metal are shown in (b) and (d).

scattering from neighboring atoms, which leads to an additional oscillatory term in the EXAFS formalism and shifts the scattering peaks, or interatomic distances, to lower values of R in $\chi(R)$.[70] The Mn–O peak at $\sim$1.4 Å remains nearly unchanged (in terms of position and amplitude) after the heat treatment, indicating that MnO_6 octahedra remain intact during the thermally-induced transformation. This is in good agreement with the lack of change in the pre-edge in the Mn XANES.[71,72] In contrast, the Mn–M peak at $\sim$2.3 Å increases in intensity, which could be related to a greater number of Mn–M correlations in the material, i.e., more Mn and/or Zr next-nearest-neighbors as scattering from Li is negligible compared to Mn and Zr.[73] Zr K-edge $\chi(R)$ results on $Li_{0.5}Mn_{0.7}Zr_{0.2}O_2$ before and after the heat treatment are presented in Fig. 4b. Similarly to the Mn K-edge data, the peaks at $\sim$1.3 Å and $\sim$2.5 Å in the data obtained before thermal relaxation correspond to nearest-neighbor (Zr–O) and next-nearest-neighbor (Zr–M, with M = Li, Mn, Zr) correlations. Upon thermal activation, the Zr–O peak both increases in intensity and shifts to a larger radial distance R. Since our earlier analysis of the diffraction results indicate that the oxygen lattice remains unchanged and Zr and Mn species remain octahedrally coordinated during the thermally-induced transformation, the enhanced Zr–O signal likely reflects a reduction in ZrO_6 octahedral distortions. Interestingly, the Zr–M peak at $\sim$2.5 Å decreases in intensity after the heat treatment, which could be related to fewer Zr–M (Zr–Mn or Zr–Zr)

correlations and contrasts with the trend in Mn–M correlations, despite Zr and Mn occupying the same crystallographic site in the average DRX structure. These results likely suggest that the increased Mn–M peak intensity primarily arises from a greater number of Mn–Mn correlations rather than Mn–Zr correlations. The presence of more Mn–Mn correlations and fewer Zr–M correlations in the material could, in principle, result from Mn species moving away from Zr species and *vice versa*. However, Zr^{4+} ions are unlikely to migrate given their higher charge and substantially larger atomic mass compared to Mn^{3+} ions. Thus, the structural reorganization is most likely driven by a redistribution of the Mn^{3+} ions within the rock salt lattice, whereby these ions move to octahedral sites that are left vacant upon Li extraction and are edge-sharing with other Mn ions.

Contrasting local structural rearrangements in $Li_{0.5}Mn_{0.7}Zr_{0.2}O_2$ and $Li_{0.5}Mn_{0.7}Ti_{0.2}O_2$

In our recent study[55] of the $Li_{1.1}Mn_{0.7}Ti_{0.2}O_2$ DRX cathode, we showed that chemical delithiation followed by a 400 °C heat treatment led to the formation of a "δ phase" comprising spinel-like ordered domains within the long-range rock salt structure. Although the short-range order that emerges from the heat treatment is similar to that observed in the case of $Li_{1.1}Mn_{0.7}Zr_{0.2}O_2$, the structural rearrangements were found to occur over much longer lengthscales in the Ti system. Here, we synthesized $Li_{1.1}Mn_{0.7}Ti_{0.2}O_2$ using a solid-state route similar to that used for $Li_{1.1}Mn_{0.7}Zr_{0.2}O_2$, and the as-prepared DRX was then

chemically delithiated to obtain $Li_{0.5}Mn_{0.7}Ti_{0.2}O_2$. Hereafter, we revisit the local structure of heat-treated $Li_{0.5}Mn_{0.7}Ti_{0.2}O_2$ using Mn K- edge EXAFS and compare it to its Zr analogue to contrast their transformation paths.

Fourier-transformed Mn K-edge EXAFS ($\chi(R)$) results on $Li_{0.5}Mn_{0.7}Ti_{0.2}O_2$ before and after a heat treatment at 400 °C are presented in Fig. 4c. The changes observed upon heating mirror those observed for the $Li_{0.5}Mn_{0.7}Zr_{0.2}O_2$ system: the Mn–O peak at ~1.3 Å remains largely unchanged, while the Mn–M (M = Li, Mn, Ti) peak at ~2.3 Å increases in intensity after the heat treatment. Once again, these observations could be related to an increased number of Mn–Mn and/or Mn–Ti next-nearest-neighbors. Additional insights into the evolution of the Mn local environments in $Li_{0.5}Mn_{0.7}Ti_{0.2}O_2$ and $Li_{0.5}Mn_{0.7}Zr_{0.2}O_2$ during thermal activation from fits of their Mn K-edge EXAFS spectra are provided in SI note S1. The Mn–M peak is consistently lower in intensity for $Li_{0.5}Mn_{0.7}Zr_{0.2}O_2$ than for $Li_{0.5}Mn_{0.7}Ti_{0.2}O_2$ (both before and after thermal activation), which likely indicates that Mn–Mn and/or Mn–Zr correlations are less favorable in the Zr system than Mn–Mn and/or Mn–Ti correlations in the Ti system. This observation agrees well with the NPDF results on as-synthesized $Li_{1.1}Mn_{0.7}Zr_{0.2}O_2$ (Fig. 1b), which revealed that Li–Mn and Li–Zr pairs preferentially form in the material.

Fourier-transformed Ti K-edge EXAFS ($\chi(R)$) results on $Li_{0.5}Mn_{0.7}Ti_{0.2}O_2$ before and after the heat treatment are shown in Fig. 4d. The Ti–O peak at ~1.2 Å slightly increases in intensity after the heat treatment, likely due to reduced lattice distortions, while the Ti–M (M = Li, Mn, Ti) peak at ~2.3 Å is dramatically enhanced, which could arise from an increased number of Ti–Ti and/or Ti–Mn next-nearest-neighbors. The evolution of the Ti local environments in $Li_{0.5}Mn_{0.7}Ti_{0.2}O_2$ during thermal activation contrasts with that of the Zr environments in $Li_{0.5}Mn_{0.7}Zr_{0.2}O_2$. As mentioned earlier, Zr species become more isolated from other TM ions in heat-treated $Li_{0.5}Mn_{0.7}Zr_{0.2}O_2$, presumably due to Mn migration away from Zr species and Mn clustering during the thermally-induced structural transformation. In contrast, the EXAFS results suggest that clusters of next-nearest-neighbor Mn and Ti ions form upon heat treatment of $Li_{0.5}Mn_{0.7}Ti_{0.2}O_2$. Given the large size of the spinel domains in this material (~20 nm),[55] the transformation likely involves migration of both Mn and Ti.

Building upon the insights obtained from EXAFS on the first few coordination shells around the TM species, NPDF was then used to probe local correlations over lengthscales up to 5 nm. Time-of-flight NPDF patterns collected on $Li_{0.5}Mn_{0.7}Zr_{0.2}O_2$ and $Li_{0.5}Mn_{0.7}Ti_{0.2}O_2$ before and after the heat treatment are shown in Fig. 5a and b over the 3.5–7.0 Å range (additional details on the NPDF analysis in SI note S2). The positive peaks at 5.1 Å, 5.9 Å, and 6.6 Å correspond to Mn–M correlations beyond the second coordination shell; amongst those, Mn–Mn correlations dominate due to the high Mn content in the systems under consideration. These correlations increase noticeably after the heat treatment for both systems, indicating some amount of Mn clustering after the structural transformation. Together, these and the Mn K-edge EXAFS results presented earlier suggest that the local structure of thermally activated $Li_{0.5}Mn_{0.7}Zr_{0.2}O_2$ and

$Li_{0.5}Mn_{0.7}Ti_{0.2}O_2$ is on average closer to that of spinel $LiMn_2O_4$ than that of a Mn-rich DRX, consistent with the electrochemical and diffraction results discussed earlier.

The full NPDF patterns collected on $Li_{0.5}Mn_{0.7}Zr_{0.2}O_2$ and plotted in Fig. S5 reveal that correlations beyond 15 Å are unaffected by the heat treatment, suggesting that the thermally-induced structural changes are confined to very small regions, in excellent agreement with the formation of ~2 nm spinel-like domains within ~180 nm grains determined from SXRD refinements. For $Li_{0.5}Mn_{0.7}Ti_{0.2}O_2$, however, the NPDF pattern changes even beyond 40 Å (the upper limit of the range probed by NPDF) during thermal activation, as shown in Fig. S6, which is consistent with our previous work where we identified the formation of a δ phase comprising coherent 6–10 nm spinel domains within ~200 nm grains for this system.[55]

Role of the d⁰ metal species on the thermally-induced structural transformation

To further explore the impact of the tetravalent d⁰ M species (Zr^{4+} vs. Ti^{4+}) on the thermally induced structural transformation, we prepared a series of chemically-delithiated $Li_{0.5}Mn_{0.7}Zr_{0.2-x}Ti_xO_2$ (x = 0, 0.05, 0.1, 0.15, and 0.2) DRX compounds using the same solid-state synthesis procedure as described earlier, and studied their structural evolution upon heating. The compositional series was chemically delithiated to a composition of $Li_{0.5}Mn_{0.7}Zr_{0.2-x}Ti_xO_2$ (ICP results in Table S1) using a similar procedure as described earlier. Due to limited access to synchrotron X-ray and neutron facilities, we prioritized the characterization of the x = 0, 0.1, and 0.2 compounds whenever needed.

Synchrotron XRD data was first collected in situ upon heating $Li_{0.5}Mn_{0.7}Zr_{0.2-x}Ti_xO_2$ (x = 0, 0.1, and 0.2) samples from room temperature to 400 °C. The results are presented as contour plots in Fig. S7 and individual diffraction patterns at select temperatures in Fig. S8. A sequential LeBail refinement of the patterns was conducted using a cubic $Fd\bar{3}m$ spinel cell to monitor the evolution of the a lattice parameter (a-parameter) during heating, shown in Fig. 6a. From room temperature up to about 130 °C, the a-parameters of $Li_{0.5}Mn_{0.7}Zr_{0.2-x}Ti_xO_2$ (x = 0, 0.1, and 0.2) increase linearly and at about the same rate, presumably due to thermal expansion. From 130 °C, a change in slope is observed for all three compounds, indicating the onset of a structural transformation. The more Ti in the DRX structure, the greater the rate of a-parameter expansion with increasing temperature, suggesting that Zr slows the phase transition relative to Ti. Additional anomalies in the rate of a-parameter expansion are noted at 250 °C and 350 °C (as indicated by the vertical dotted lines in Fig. 6a), and consistently observed across the series, implying that the structural transformation takes place in distinct stages.

From the onset of the transformation at 130 °C, the diffuse scattering peaks gradually become more intense, particularly at 1.3 Å. For the Zr-only, x = 0 compound, the broad peaks are extremely weak and grow at a slow rate. As the Zr content decreases across the series, the broad peaks become more prominent and grow at a faster rate upon heating. For the x =
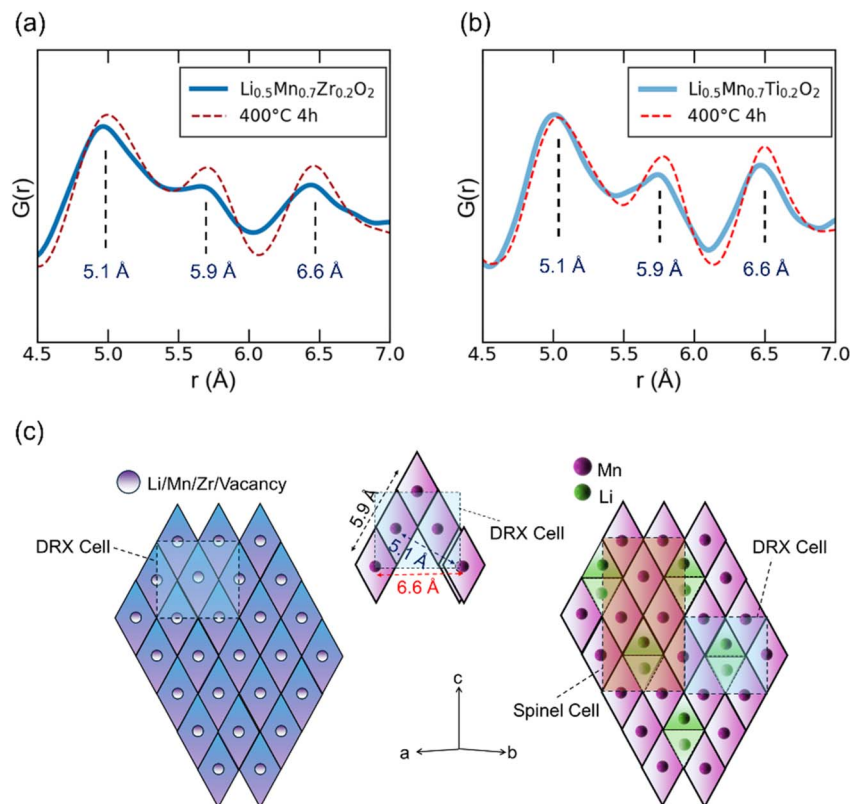
Fig. 5 Neutron PDF of the chemically delithiated (a) $Li_{0.5}Mn_{0.7}Zr_{0.2}O_2$ and (b) $Li_{0.5}Mn_{0.7}Ti_{0.2}O_2$ DRX before and after a 400 °C heat treatment for 4 h. (c) Illustration of Mn clustering in the rock salt structure to form spinel-like features.

0.2 compound, where Zr is entirely replaced by Ti, the diffuse scattering peaks eventually sharpen beyond 200 °C, indicating the formation of large spinel domains characteristic of the δ phase.[50,55,57,62,74] Once again, we use a "spinel domain" structural model for the sequential Rietveld refinement of the *in situ* patterns collected on the three compounds and track the evolution of the spinel domain size. Fig. 6b illustrates the ratio

of the average spinel domain size to the average bulk grain size, with the domain and grain sizes obtained from the width of the diffuse scattering peaks and sharp reflections, respectively. Spinel domains start to grow at 130 °C for all $Li_{0.5}Mn_{0.7}$-$Zr_{0.2-x}Ti_xO_2$ compounds, and grow more rapidly and reach a larger size as the Ti content (x) increases, mirroring the trends observed in a-lattice parameter expansion.
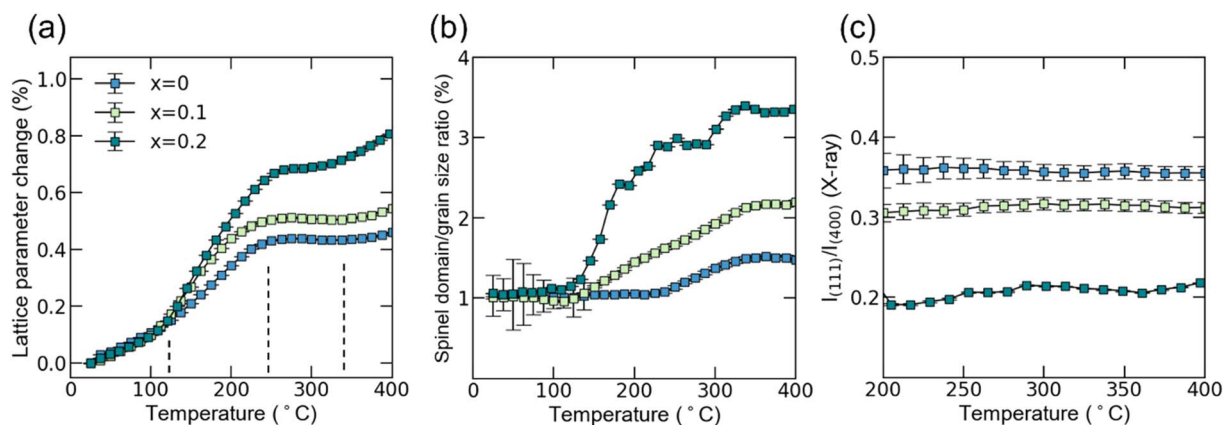

Fig. 6 Monitoring the thermally-induced structural transformation in $Li_{0.5}Mn_{0.7}Zr_{0.2-x}Ti_xO_2$ ($x = 0$, 0.1, and 0.2) compounds using SXRD with *in situ* heating from room temperature to 400 °C ((a)–(c)). (a) A lattice parameter evolution, (b) ratio of the average spinel domain size to the average grain size, and (c) ratio of the (111) peak intensity ($I_{(111)}$) to the (400) peak intensity ($I_{(400)}$) upon heating. The $I_{(111)}/I_{(400)}$ ratio is indicative of the relative occupancy of the 16c and 16d octahedral sites.

In the spinel structure, the reflection at 1.3 Å^{-1} corresponds to the (111) planes, and its relative intensity compared to the reflection at ~3 Å^{-1} arising from the (400) planes has been used to monitor the development of cation short-range order during the transition from cubic rock salt to spinel.[75] The appearance of the (111) reflection, whether as diffuse scattering or a sharp peak, indicates cation ordering amongst the distinct 16c and 16d octahedral sites of the spinel structure. Since XRD is primarily sensitive to heavy elements, the ratio $I_{(111)}/I_{(400)}$, plotted as a function of temperature in Fig. 6c, mainly reflects the relative occupancy of these sites by Mn, Zr, and Ti. The (111) peak is too broad to be fit accurately below 200 °C; thus, only the data acquired above 200 °C is analyzed here. The ratio $I_{(111)}/I_{(400)}$ remains relatively constant across the entire temperature range for all samples, indicating that TM migration mostly takes place during the low-temperature structural transition between 130 °C and 200 °C. While no significant cation rearrangements occur above 200 °C, small spinel domains coalesce into larger ordered regions, and for the $x = 0.2$ compound, evolve into nano-domains with a refined crystal size of ~10 nm at 400 °C.

To obtain additional insight into the evolution of the local structure during heating, NPDF data was collected on $x = 0$, 0.1, and 0.2 samples equilibrated at 25, 100, 200, 300, and 400 °C, and is shown in Fig. S9–S11. The magnitude of the structural changes taking place over the 25–100 °C, 100–200 °C, 200–300 °C, and 300–400 °C temperature intervals was quantified from the NPDF patterns as described in SI note S3 and shown in Fig. S12. We find that the evolution of the local structure of $Li_{0.5}Mn_{0.7}Zr_{0.2}O_2$ is more subtle and occurs over much shorter lengthscales compared to $Li_{0.5}Mn_{0.7}Zr_{0.1}Ti_{0.1}O_2$ and $Li_{0.5}Mn_{0.7}Ti_{0.2}O_2$, confirming that Zr incorporation impedes the formation of large spinel-ordered domains.

Next, $Li_{0.5}Mn_{0.7}Zr_{0.2-x}Ti_xO_2$ samples obtained after a 4 h heat treatment at 400 °C were characterized using SXRD for all compositions ($x = 0$, 0.05, 0.1, 0.15 and 0.2), and NPD for the $x = 0$, 0.1, and 0.2 compounds. The ratio of the average spinel domain size to the average grain size derived from the Rietveld refinements of the SXRD and NPD patterns is plotted as a function of x in Fig. 7. The trend across the different compositions is broadly consistent with that obtained from the *in situ* SXRD data on the $x = 0$, 0.1, and 0.2 compounds,

indicating that the spinel domains decrease in size as the Zr content increases. Interestingly, the impact of the Zr content on the average size of the spinel domains is not linear with x: even a small amount of Zr ($Zr_{0.05}$) dramatically reduces the size of the domains, and increasing the Zr content beyond $Zr_{0.1}$ does not appear to lead to further shrinkage of the already very small domains. A recent computational study suggested that the relatively low mobility of Ti^{4+} compared with Mn can impede the growth of spinel domains in Mn-rich DRX,[76] explaining the observed plateau in domain growth during electrochemical cycling[77] or low-temperature (200 °C) annealing.[57] We find that spinel domains are larger (~20 nm) and more crystalline in the $x = 0.2$ sample heat-treated at 400 °C for 4 h than in the same composition examined *in situ* during heating to 400 °C (~10 nm), presumably due to the longer dwell time at elevated temperature. In contrast, in compounds containing Zr, the spinel domain size does not change appreciably with dwell time at 400 °C. These findings indicate that, given sufficient time, Ti^{4+} migration occurs at 400 °C, whereas Zr^{4+} migration remains very limited and thus exerts a stronger pinning effect on domain growth. Refinements of the NPD patterns reveal a decrease in the occupation of the tetrahedral Li sites in the spinel domains with increasing Zr content, as shown in Fig. 7.

Finally, ^7Li solid-state NMR measurements were performed on the entire $Li_{0.5}Mn_{0.7}Zr_{0.2-x}Ti_xO_2$ series before and after a heat treatment at 400 °C for 4 h to better understand the impact of Zr and Ti on the evolution of the Li environments. We note that the NMR shift of a ^7Li species in paramagnetic $Mn^{3+/4+}$-containing materials depends on the number and oxidation state of neighboring Mn ions, and the geometry of Li–O–Mn interaction pathways (bond angles and bond lengths). Hence, NMR provides detailed insight into the distribution of local environments in the materials before and after thermal relaxation. The ^7Li spectra are presented in Fig. S13 and described in detail in SI note S4. The broad resonance at ~700 ppm observed for all $Li_{0.5}Mn_{0.7}Zr_{0.2-x}Ti_xO_2$ compounds prior to the heat treatment reveals a broad distribution of octahedral Li environments in the paramagnetic DRX cathodes.[54,55] Sharper ^7Li resonances are observed for all heat-treated compounds (and in particular for the $x > 0.1$ systems), indicating a narrower distribution of Li environments, *i.e.*, greater cation ordering, in the transformed structures. For the $x \geq 0.15$ compounds, a prominent resonance emerges at ~520 ppm, which we attribute to Li in tetrahedral (8a), spinel $LiMn_2O_4$-like environments.[78–80] In contrast, the spectra obtained on the thermally activated $x \leq 0.1$ compounds comprise a main resonance at approximately the same shift as that present prior to the heat treatment (~700 ppm), but slightly sharper, and only a small shoulder at ~520 ppm, suggesting that Li species mostly remain octahedrally coordinated in the spinel domains. Based on prior NMR studies of $LiMn_{2-x}Ti_xO_4$ (ref. 79) and $Li_2Mn_2O_4$,[78,81] we estimate the shift of a Li in a regular octahedral site (*e.g.* 16d) in the spinel structure and surrounded by 6 nearest-neighbor Mn^{4+} (in adjacent 16c sites) to be around 1100 ppm, while that for 16d Li surrounded by 6 Mn^{3+} to be closer to 100 ppm.[79] Hence, the observed intermediate 700 ppm shift is in line with that expected for 16d Li
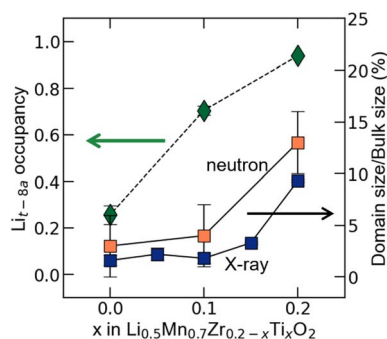

Fig. 7 Ratio of the average spinel domain size to the average grain size from *ex situ* SRXD, and tetrahedral Li site occupancy from *ex situ* NPD, for $Li_{0.5}Mn_{0.7}Zr_{0.2-x}Ti_xO_2$ samples equilibrated at 400 °C for 4 h.

surrounded by 6 Mn with an average oxidation state of +3.86 as in $Li_{0.5}Mn_{0.7}Zr_{0.2}O_2$. Similarly to the initial DRX cathodes, the rather broad 700 ppm resonance observed for the thermally-activated $x \leq 0.1$ compounds indicates a distribution of Li environments in the spinel domains, which could arise from structural strain (due to the small domain size) and residual cation disorder. Furthermore, the low frequency tail observed below 400 ppm in all spectra collected after thermal activation could result from Li in octahedral (16d) or tetrahedral (8a) sites with one or more nearest-neighbor diamagnetic species (Zr^{4+}, Li^+ or vacancies). The ^7Li NMR results are overall in good agreement with the NPD results and suggest that the structural rearrangements taking place in the Ti-rich compounds lead to significant migration of Li species from octahedral to tetrahedral sites, whereas the majority of the Li remains octahedrally coordinated in the Zr-rich compounds.

Impact of the d^0 metal and thermal activation on the electrochemical performance

In this section, we compare the half-cell electrochemical performance over the first 50 cycles of $Li_yMn_{0.7}Zr_{0.2-x}Ti_xO_2$ ($y = 1.1$ and 0.5, $x = 0$, 0.05, 0.1, 0.15, and 0.2) composite cathodes prepared by hand grinding the active material (DRX powder) with carbon during electrode fabrication, to evaluate the impact, at a constant Mn content, of the d^0 metal and of thermal activation on the electrochemical performance.

The electrochemical profiles obtained for the as-synthesized DRX compounds are presented in Fig. S14. The Zr-rich $x = 0$ and 0.05 cathodes show almost no evolution in the shape of their electrochemical profiles and gradual capacity decay (Fig. S14a and b), suggesting no bulk structural rearrangements upon cycling. In contrast, the more Ti-rich $x = 0.1$, 0.15, and 0.2 cathodes all show clear capacity activation (Fig. S14c–e), with the growth of electrochemical plateaus at 3 and 4 V vs. Li/Li^+ during cycling. For $Li_{1.1}Mn_{0.7}Ti_{0.2}O_2$ ($x = 0.2$), capacity activation has been attributed to a bulk δ phase transition with the formation of large (~10 nm-sized) and coherent spinel-like structural domains within the long-range DRX structure,[54] which is similar to the structure that forms after chemical delithiation and a 400 °C heat treatment.[55] Overall, these electrochemical results reveal that the rate and extent of the structural rearrangements taking place during electrochemical cycling strongly depend on the nature of the d^0 species (here, the Zr : Ti ratio), in addition to the dependence on the Mn content noted in earlier work.[54]

We now compare the electrochemical performance of the chemically-delithiated $Li_{0.5}Mn_{0.7}Zr_{0.2-x}Ti_xO_2$ DRX, with electrochemical profiles presented in Fig. S15. Once again, the Zr-rich $x = 0$ and 0.05 cathodes exhibit only very small changes in the shape of their electrochemical profiles and negligible capacity activation (capacity < 20 mAh g^{-1} throughout cycling). In contrast, the $x = 0.1$, 0.15, 0.2 cathodes show capacity activation with spinel-like pseudo-plateaus gradually emerging at 3 and 4 V. The capacities observed for the chemically-delithiated $Li_{0.5}Mn_{0.7}Zr_{0.2-x}Ti_xO_2$ cathodes are always lower (all <55 mAh g^{-1}) than those observed for the as-synthesized compounds (up

to >80 mAh g^{-1} after 50 cycles for the $x = 0.2$ cathode), which could be due to surface structural changes taking place during the reaction with the NO_2BF_4 oxidizing agent.

After a 400 °C heat treatment for 4 h, the shape of the electrochemical profile significantly changes and the capacity is significantly enhanced (up to 8-fold) for all $Li_{0.5}Mn_{0.7}Zr_{0.2-x}Ti_xO_2$ cathodes, as shown in Fig. S16. Yet, the achievable capacity still decreases with decreasing Ti content (x), from ~200 mAh g^{-1} (exchange of 0.6 Li per formula unit) for the $x = 0.2$ cathode to ~140 mAh g^{-1} (exchange of 0.4 Li per formula unit) for the $x = 0$ cathode.

The rate performance of the thermally-activated $Li_{0.5}Mn_{0.7}Zr_{0.2-x}Ti_xO_2$ compounds was tested using galvanostatic cycling at various current densities from 20 mA g^{-1} to 1 A g^{-1}, with results shown in Fig. 8a. Overall, the rate performance of all cathodes is quite poor even after the thermally-induced phase transition. It is obvious that a lower Zr content or higher Ti content leads to a higher capacity at all current densities.

GITT measurements were conducted on the heat-treated $x = 0$, 0.1 and 0.2 cathodes during the second charge–discharge cycle, and the results are presented in Fig. 8b. The measurements reveal comparable polarization and voltage hysteresis for all three compounds. Both the hysteresis and overpotential are most pronounced between 3 and 4 V (excluding the ~3 V plateau), likely reflecting the sluggish redistribution of Li ions between tetrahedral and octahedral sites within the spinel domains in this voltage range, similar to that observed in $Li_yMn_2O_4$ spinel cathodes.[68,82,83]

A detailed analysis of the GITT results is precluded by the possible two-phase reaction mechanisms occurring during (de) lithiation of $Li_{0.5}Mn_{0.7}Zr_{0.2-x}Ti_xO_2$ compounds with sufficiently large spinel domains. However, comparison of the IR drop in the low-potential region (<3 V), where Li ions mainly occupy octahedral sites, and in the high-potential region (>4 V), where Li mainly occupy tetrahedral sites, indicates that the Zr : Ti ratio does not significantly affect the overpotential (Fig. S17). This suggests that contact, electronic, and charge-transfer resistances are comparable across all three DRX compositions and are unlikely to explain the observed performance differences. While prior studies have indicated that the electronic conductivity[84] of DRX cathodes depends on composition (and likely short-range cation order), the high carbon content (20 wt%) in the composite cathodes used here likely minimizes such differences. Hence, ion transport limitations appear to dominate the rate performance of the thermally activated $Li_{0.5}Mn_{0.7}Zr_{0.2-x}Ti_xO_2$ compounds, becoming more pronounced as the Zr content increases.

Discussion

Thermodynamic driving force for structural rearrangements in $Li_{1.1}Mn_{0.7}Zr_{0.2}O_2$ versus $Li_{1.1}Mn_{0.7}Ti_{0.2}O_2$

Although the $Li_{1.1}Mn_{0.7}Zr_{0.2}O_2$ ($x = 0$) DRX cathode does not transform during electrochemical cycling, local structural rearrangements (<20 Å) can be induced through chemical delithiation and a 400 °C heat treatment for 4 h. This is in contrast to the $Li_{1.1}Mn_{0.7}Ti_{0.2}O_2$ ($x = 0.2$) cathode, which

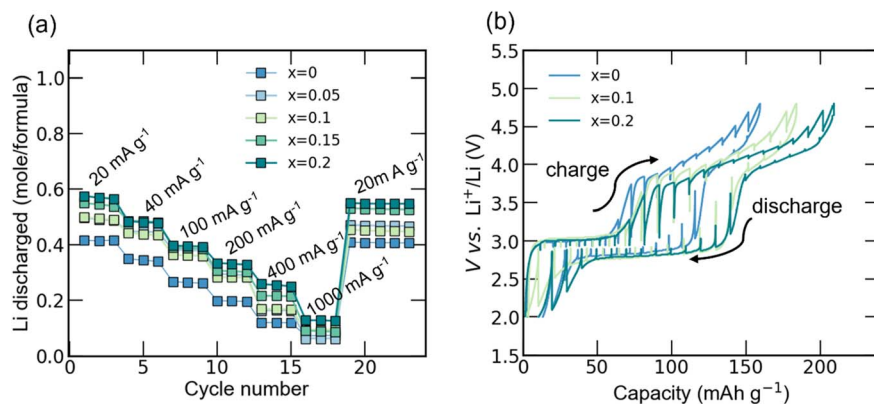Fig. 8 (a) Rate capability tests at 25 °C of thermally activated $Li_{0.5}Mn_{0.7}Zr_{0.2-x}Ti_xO_2$ (x = 0, 0.05, 0.1, 0.15, and 0.2) over the 4.8–2 V window, and (b) select galvanostatic intermittent titration technique (GITT) curves of thermally activated $Li_{0.5}Mn_{0.7}Zr_{0.2-x}Ti_xO_2$ (x = 0, 0.1 and 0.2), where the cells were charged or discharged at 20 mA g^{-1} for 30 minutes, followed by a 16-hour open-circuit relaxation step that was found to be sufficiently long to allow the system to equilibrate at each step.

undergoes a long-range δ phase transition both during electrochemical cycling[54,57] and when subjected to the chemical and heat treatment described above.[55] This leads us to compare the thermodynamic driving force for structural rearrangements in these two systems, to shed light on their contrasting behaviors.

To better understand the thermodynamic driving force towards structural rearrangements in the Zr system, oxide melt drop solution calorimetry[85] was conducted on chemically delithiated $Li_{0.5}Mn_{0.7}Zr_{0.2}O_2$ before and after a 400 °C heat treatment to extract the enthalpy of formation from oxides and O_2 ($\Delta H^{\circ}_{f,ox\ 298K}$), with results shown in Fig. 9. A formation enthalpy of -43.6 ± 2.6 kJ mol^{-1} is obtained for chemically delithiated $Li_{0.5}Mn_{0.7}Zr_{0.2}O_2$, which becomes more negative (-53.3 ± 1.9 kJ mol^{-1}) after the heat treatment. Hence, the thermodynamic driving force for the observed structural rearrangements is -9.7 ± 3.2 kJ mol^{-1}. For comparison, we also show our previously reported[55] results on $Li_{0.5}Mn_{0.7}Ti_{0.2}O_2$ in Fig. 9. A formation enthalpy of -44.1 ± 1.2 kJ mol^{-1} was obtained for chemically delithiated $Li_{0.5}Mn_{0.7}Ti_{0.2}O_2$, and of -63.5 ± 1.6 kJ mol^{-1} after the heat treatment, resulting in

a thermodynamic driving force of -19.4 ± 2.0 kJ mol^{-1} for the observed structural rearrangements. These two thermodynamic driving forces are not directly comparable given the slightly different Li contents and the different degrees of structural transformation in the two systems. However, a thermodynamic driving force of -9.7 ± 3.2 kJ mol^{-1} is sufficiently large to result in a large equilibrium constant for the forward structural transformation in $Li_{1.1}Mn_{0.7}Zr_{0.2}O_2$, suggesting that the structural transformation is thermodynamically favorable but could be kinetically limited during electrochemical cycling.

Role of Zr on the phase transformation

Previous studies have identified the overall Mn content as a key factor influencing the rate and extent of the bulk δ phase transition observed in Mn-rich DRX cathodes during electrochemical cycling.[54,55] This work reveals that the d^0 metal also plays a significant role in the transformation. We have found that increasing the Zr content at a constant Mn content slows or even prevents structural rearrangements during cycling in $Li_{1.1}Mn_{0.7}Zr_{0.2-x}Ti_xO_2$ compounds. We have also shown that, when chemically delithiated $Li_{0.5}Mn_{0.7}Zr_{0.2-x}Ti_xO_2$ samples are heated from room temperature to 400 °C, spinel-like atomic correlations emerge within the long-range DRX structure starting at ∼130 °C irrespective of the Zr : Ti ratio. However, with increasing Zr content, the structural transformation (Fig. 6a) and growth of the spinel domains (Fig. 6b) proceed at a slower rate on heating. This trend is confirmed by our analysis of $Li_{0.5}Mn_{0.7}Zr_{0.2-x}Ti_xO_2$ samples equilibrated at 400 °C for 4 h, indicating that the correlation length of the emerging spinel domains is significantly reduced when even a small amount of Zr ($Zr_{0.05}$) is incorporated into structure. Interestingly, both NPD and ^7Li NMR results suggest that the occupation of tetrahedral sites by Li in thermally activated $Li_{0.5}Mn_{0.7}Zr_{0.2-x}Ti_xO_2$ is positively correlated with the size of the spinel domains that emerge during the heat treatment (thus, inversely correlated with the amount of Zr in the material); a similar trend between tetrahedral cation site occupancy and domain size has been
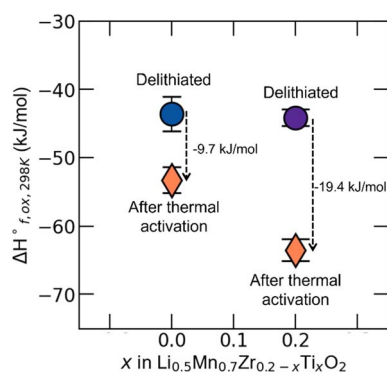

Fig. 9 Enthalpy of formation from binary oxides and oxygen of chemically delithiated $Li_{0.5}Mn_{0.7}Zr_{0.2}O_2$ and $Li_{0.5}Mn_{0.7}Ti_{0.2}O_2$ before and after a 400 °C heat treatment for 4 h.

reported for Fe_xO compounds exhibiting a spinel–rock salt domain structure.[86]

The growth of spinel domains within the partially delithiated DRX structure depends on the migration of TM species from their original octahedral sites to adjacent octahedral sites left vacant upon Li extraction.[55] The Mn, Ti and Zr K-edge EXAFS results presented here (Fig. 4) clearly indicate that Mn and Ti local environments evolve similarly in $Li_{0.5}Mn_{0.7}Ti_{0.2}O_2$, unlike Mn and Zr environments in $Li_{0.5}Mn_{0.7}Zr_{0.2}O_2$. Specifically, the EXAFS data suggests the formation of clusters of next-nearest-neighbor Mn and Ti species in thermally activated $Li_{0.5}Mn_{0.7}Ti_{0.2}O_2$. If Ti were completely immobile during the transformation, the resulting spinel domains would be limited to approximately 3–4 unit cells ($\sim$2 nm). However, domains as large as 20 nm form after a annealing at 400 °C for 4 h, indicating that both Mn and Ti species participate in the migration process. This observation is consistent with our previous findings that, after a 400 °C heat treatment, Mn and Ti preferentially occupy one of the two octahedral sites in the spinel structure, leaving the other site nearly vacant.[55] In contrast, Zr K-edge EXAFS results reveal that Zr species become more isolated from other TM ions in thermally activated $Li_{0.5}Mn_{0.7}Zr_{0.2}O_2$. Although these results do not provide direct evidence for or against Zr migration during the structural transformation, since the observed evolution of the average Zr local environment could result from the movement of Zr and/or of neighboring Mn species, Zr^{4+} migration is likely a rare event compared to Mn^{4+} and Ti^{4+} migration. This is consistent with the significantly larger ionic radius (0.72 Å) and mass (91 amu) of Zr^{4+} relative to Mn^{4+} (0.53 Å, 55 amu) and Ti^{4+} (0.605 Å, 48 amu). Moreover, Mn^{4+} migrates more readily than Ti^{4+}, as evidenced by the faster δ phase transition in $Li_{1.1}Mn_{0.9}O_2$ compared with $Li_{1.1}Mn_{0.8}Ti_{0.1}O_2$ during cycling.[87] The presence of isolated Zr species and clustered Mn species in heat-treated $Li_{0.5}Mn_{0.7}Zr_{0.2}O_2$ suggests that the resulting spinel domains are Mn-rich, with Zr species delineating the boundaries between them—consistent with the distribution of Li environments observed by NMR—and thereby constraining further domain growth.

Despite the in-depth structural analysis conducted in this work, identifying the role of Zr on the extent of the phase transformation during thermal activation remains challenging given the very similar DRX and (partially disordered) spinel structures, both at the long-range and in terms of their possible distributions of Li environments. In contrast, the electrochemical profiles of the thermally activated cathodes provide a unique window on the extent of the local structural rearrangement. In particular, the proportion of DRX phase remaining in the heat-treated $Li_{0.5}Mn_{0.7}Zr_{0.2-x}Ti_xO_2$ cathodes can be inferred from the slope of the voltage profiles. Given that our as-synthesized DRX cathodes exhibit a sloping voltage profile over the entire voltage range, with no electrochemical plateau (see the first few cycles for each composition in Fig. S14), any remaining DRX phase in the thermally activated cathodes should introduce some slope to the electrochemical profile. Instead, we find that the electrochemical curves of all thermally activated $Li_{0.5}Mn_{0.7}Zr_{0.2-x}Ti_xO_2$ cathodes exhibit a long and relatively flat plateau at 3 V (Fig. S16), indicative of a nearly complete transformation of the local structure into a well-ordered spinel, irrespective of the Zr content. Nevertheless, ^{7}Li ssNMR spectra reveal some fraction of disordered rock salt-like Li environments in all thermally relaxed compounds (Fig. S13). Those disordered regions may reside at the d^0-rich domain boundaries, as previously proposed by Ceder and coworkers.[57,76] A similar complete conversion of the $Li_{1.2}Mn_{0.65}Ti_{0.15}O_{1.9}F_{0.1}$ DRX to a spinel domain structure with TM cations occupying either the 16c or 16d octahedral sites was reported by Ceder and coworkers[57] after chemical delithiation and a heat treatment.

Impact of Zr content on long-range Li-ion transport and electrochemical performance

We now connect the local structure of $Li_yMn_{0.7}Zr_{0.2-x}Ti_xO_2$ DRX cathodes in the pristine, chemically delithiated, and thermally activated state and their electrochemical performance.

Reversible Li extraction from intercalation electrode materials relies on the presence of Li-ion conduction pathways percolating through the particles. Even at a slow cycling rate of 20 mAh g^{-1} (roughly C/10), we find that as-synthesized $Li_{1.1}Mn_{0.7}Zr_{0.2-x}Ti_xO_2$ and chemically delithiated $Li_{0.5}Mn_{0.7}Zr_{0.2-x}Ti_xO_2$ DRX cathodes hand ground with carbon (no particle downsizing) lead to very low capacities, which we attribute to poorly connected Li-ion diffusion channels due to the approximately random distribution of Li and TM species, and long diffusion paths across the very large particles (on the order of tens of microns). Remarkably, a relatively mild heat treatment at 400 °C for 4 h yields up to an eight-fold increase in capacity across all chemically delithiated $Li_{0.5}Mn_{0.7}Zr_{0.2-x}Ti_xO_2$ compositions studied. Such pronounced improvements indicate that thermal activation generates a structure with substantially enhanced interconnectivity of Li-ion transport channels. This enhancement arises from the formation of spinel domains featuring 3D networks of 0-TM channels, where face-sharing octahedral (16d) and tetrahedral (8a) sites are alternately occupied by Li or vacant, while TM ions reside on 16c octahedral sites, thus enabling efficient long-range Li-ion transport.[88–90] Differences in interconnectivity of Li-ion transport channels in the DRX and spinel oxide structures are illustrated in Fig. 10a and b.

Although all $Li_{0.5}Mn_{0.7}Zr_{0.2-x}Ti_xO_2$ compounds undergo a structural transition during heat treatment, the achievable capacity decreases with increasing Zr content, from $\sim$200 mAh g^{-1} (0.6 Li per formula) for $Li_{0.5}Mn_{0.7}Ti_{0.2}O_2$ to $\sim$140 mAh g^{-1} (0.4 Li per formula) for $Li_{0.5}Mn_{0.7}Zr_{0.2}O_2$. This trend can be understood through the spinel domain structural model proposed by Ceder and coworkers.[57] In this model, spinel domains formed during cycling or a heat treatment are separated by antiphase boundaries, as illustrated in Fig. 10d and e. Our characterization of the thermally activated $Li_{0.5}Mn_{0.7}Zr_{0.2-x}Ti_xO_2$ series is consistent with this framework suggesting a homogeneous phase transformation in which the size of the emerging spinel domains depends on the Zr : Ti ratio.
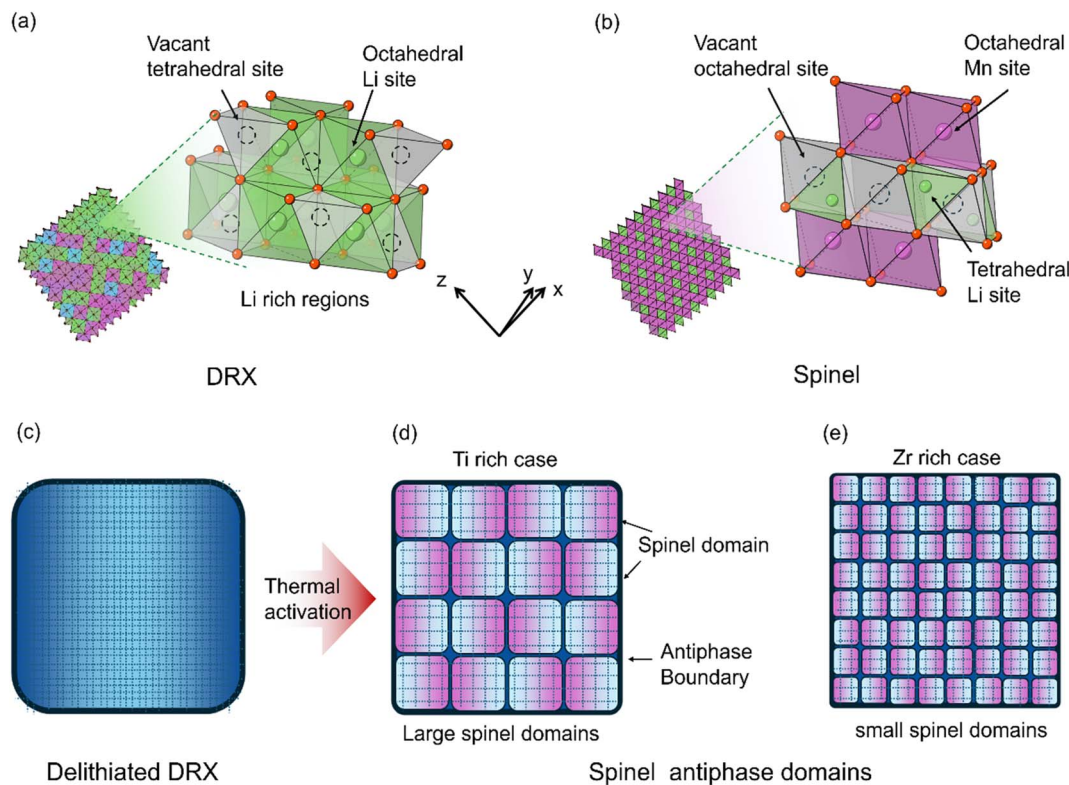
Fig. 10 Connectivity of Li–ion transport channels in (a) DRX and (b) spinel oxide structures. Illustration of conversion of (c) delithiated DRX into spinel domains with (d) large and (e) small domain sizes separated by antiphase boundaries.

Within these thermally activated structures, Li-ion diffusion occurs both inside the spinel domains and across the antiphase boundaries. However, the boundaries are more disordered and contain fewer 0-TM channels,[76] resulting in poorer Li-ion transport relative to the domain interiors and making transport across boundaries rate-limiting. We further propose that electron scattering is more likely to happen at the domain boundaries, which are d^0-rich and Mn-poor—factors that further impede electronic conductivity. Overall, the reduced performance of Zr-rich $Li_{0.5}Mn_{0.7}Zr_{0.2-x}Ti_xO_2$ systems can be attributed to their smaller spinel domains and higher density of Zr-rich antiphase boundaries, which hinder Li-ion and, potentially, electron transport compared to Ti-rich systems.

Finally, it has been suggested[57,76] that the nanosized spinel domains formed in Mn-rich DRX can suppress both the cubic-to-tetragonal phase transition and the collective Jahn–Teller distortion that occur in bulk spinel $LiMn_2O_4$ during cycling, thereby enhancing cycling stability. Consequently, controlling the size of the spinel domains in DRX through compositional of d^0 TMs represents a strategy to optimize long-term performance.

Conclusion

This work demonstrates that the electrochemical performance of Mn-rich disordered rock salt (DRX) oxide cathodes can be significantly enhanced by inducing a local phase transformation through combined chemical and thermal treatment.

Notably, it shows that local cation ordering over lengthscales <20 Å can be at least as important as the long-range (average) crystal structure in determining the Li (de)intercalation behavior of the electrode. Focusing on the $Li_{1.1}Mn_{0.7}Zr_{0.2-x}Ti_xO_2$ series, we demonstrated that the relative ratio of the hypervalent (d^0) Ti^{4+} and Zr^{4+} species strongly influences the growth of spinel-like domains during a 400 °C anneal, with direct consequences for electrochemical performance.

While Zr-rich $Li_xMn_{0.7}Zr_{0.2}O_2$ cathodes exhibit limited capacity, a 400 °C heat treatment following chemical delithiation results in a remarkable seven-fold capacity enhancement, without altering the composition and long-range crystal structure. Mn K-edge EXAFS and neutron pair distribution function analyses indicate that this capacity enhancement is associated with the formation of spinel-like cation order within nanoscale domains. Mn, Ti and Zr K-edge EXAFS measurements reveal that, during thermal treatment, Mn and Ti species cluster to form spinel domains in $Li_{0.5}Mn_{0.7}Ti_{0.2}O_2$, whereas Zr species in $Li_{0.5}Mn_{0.7}Zr_{0.2}O_2$ become more isolated from other transition metals.

A systematic investigation of thermally-induced structural rearrangements in the $Li_{0.5}Mn_{0.7}Zr_{0.2-x}Ti_xO_2$ series indicated that even small amounts of Zr ($Zr_{0.05}$) significantly slow the phase transformation and the growth of spinel domains. Nevertheless, substantial capacity enhancements are observed for all compositions, regardless of the size of the spinel domains that emerge during thermal activation. The shape of

the electrochemical profiles further suggest nearly complete conversion into ordered spinel domains.

We reconcile these observations by proposing that thermally activated $Li_{0.5}Mn_{0.7}Zr_{0.2-x}Ti_xO_2$ compounds consist of Li-conductive spinel-like domains separated by poorly conducting antiphase boundaries. Thermally-activated $Li_{0.5}Mn_{0.7}Ti_{0.2}O_2$ exhibits the highest capacity, likely due to the formation of large spinel domains separated by relatively few antiphase boundaries, enabling fast bulk Li-ion transport. In contrast, for $x < 0.2$, smaller spinel domains emerge that are delineated by Zr-rich antiphase boundaries that impede Li-ion and possibly electron transport, explaining the progressive decline in performance with increasing Zr content even after thermal activation.

Author contributions

T. L. – conceptualization, methodology, formal analysis, investigation, visualization, writing – original draft; O. M. – investigation, data analysis, writing, editing; T. S. G – investigation, data analysis and editing; E. A. L. – investigation, data analysis and editing; A. Z. – investigation and data analysis; J. L. – investigation and data analysis; E. A. – investigation; A. N. – supervision, review and editing; J. N. W– supervision, review and editing; R. J. C. – conceptualization, funding acquisition, supervision, writing, review and editing.

Conflicts of interest

The authors declare no competing financial interest.

Data availability

Raw data can be obtained by sending direct requests to the corresponding author.

The data supporting this article has been included in the supplementary information (SI). Supplementary information: description of material synthesis procedures, characterization methods, and electrochemical tests. Tables of crystal structure parameters obtained from Rietveld refinements. Table summarizing the chemical composition of $Li_yMn_{0.7}Zr_{0.2-x}Ti_xO_2$ samples before and after chemical delithiation, as obtained from ICP. Table of structural parameters obtained from fits of the Mn K-edge EXAFS data collected on $Li_{0.5}Mn_{0.7}Zr_{0.2-x}Ti_xO_2$ samples before after the heat treatment. Technical details and additional analysis of EXAFS spectra. Additional details on the analysis of the ^7Li solid-state NMR spectra obtained on $Li_{0.5}Mn_{0.7}Zr_{0.2-x}Ti_xO_2$ samples before and after the heat treatment. Additional details on in-situ neutron PDF analysis of $Li_{0.5}Mn_{0.7}Zr_{0.2-x}Ti_xO_2$ samples. Small box fits of time-of-flight neutron PDF data collected on as-synthesized $Li_{1.1}Mn_{0.7}Zr_{0.2}O_2$. SEM images of $Li_{1.1}Mn_{0.7}Zr_{0.2}O_2$ before and after ball-milling. Comparison of neutron PDF patterns obtained on $Li_{0.5}Mn_{0.7}Zr_{0.2-x}Ti_xO_2$ samples heated at different temperatures and summed differences between temperature intervals. Neutron diffraction pattern collected on $Li_{0.5}Mn_{0.7}Zr_{0.2}O_2$ after the heat treatment, along with the Rietveld refinement fit. Fits of Mn K-edge EXAFS data collected on $Li_{0.5}Mn_{0.7}Zr_{0.2-x}Ti_xO_2$ samples before after the heat treatment. Contour plots of the *in situ* synchrotron XRD data as well as individual diffraction patterns at selected temperatures obtained upon heating $Li_{0.5}Mn_{0.7}Zr_{0.2-x}Ti_xO_2$ samples. ^7Li solid-state NMR spectra collected on $Li_{0.5}Mn_{0.7}Zr_{0.2-x}Ti_xO_2$ samples before and after a 400 °C heat treatment for 4 h. Electrochemical profiles of as-synthesized $Li_{1.1}Mn_{0.7}Zr_{0.2-x}Ti_xO_2$ and $Li_{0.5}Mn_{0.7}Zr_{0.2-x}Ti_xO_2$ before and after heat treatment. IR drop observed during a GITT measurement on thermally activated $Li_{0.5}Mn_{0.7}Zr_{0.2-x}Ti_xO_2$. See DOI: **https://doi.org/10.1039/d5sc06959a**.

References

1 A. Manthiram, A Reflection on Lithium-Ion Battery Cathode Chemistry, *Nat. Commun.*, 2020, **111**(11), 1–9.

2 M. S. Whittingham, Lithium Batteries and Cathode Materials, *Chem. Rev.*, 2004, **104**, 4271–4301.

3 C. Liu, Z. G. Neale and G. Cao, Understanding Electrochemical Potentials of Cathode Materials in Rechargeable Batteries, *Mater. Today*, 2016, **19**, 109–123.

4 X. Ma, X. Cao, Y. Zhou, S. Guo, X. Shi, G. Fang, A. Pan, B. Lu, J. Zhou and S. Liang, Tuning Crystal Structure and Redox Potential of NASICON-Type Cathodes for Sodium-Ion Batteries, *Nano Res.*, 2020, **13**, 3330–3337.

5 G. L. Xu, R. Amine, Y. F. Xu, J. Liu, J. Gim, T. Ma, Y. Ren, C. J. Sun, Y. Liu, X. Zhang, S. M. Heald, A. Solhy, I. Saadoune, W. L. Mattis, S. G. Sun, Z. Chen and K. Amine, Insights into the Structural Effects of Layered Cathode Materials for High Voltage Sodium-Ion Batteries, *Energy Environ. Sci.*, 2017, **10**, 1677–1693.

6 G. Yang, H. Ni, H. Liu, P. Gao, H. Ji, S. Roy, J. Pinto and X. Jiang, The Doping Effect on the Crystal Structure and Electrochemical Properties of $LiMn_xM_{1-x}PO_4$ (M = Mg, V, Fe, Co, Gd), *J. Power Sources*, 2011, **196**, 4747–4755.

7 C. Zhang, R. Gao, L. Zheng, Y. Hao and X. Liu, New Insights into the Roles of Mg in Improving the Rate Capability and Cycling Stability of $O3-NaMn_{0.48}Ni_{0.2}Fe_{0.3}Mg_{0.02}O_2$ for Sodium-Ion Batteries, *ACS Appl. Mater. Interfaces*, 2018, **10**, 10819–10827.

8 C. Cui, X. Fan, X. Zhou, J. Chen, Q. Wang, L. Ma, C. Yang, E. Hu, X. Q. Yang and C. Wang, Structure and Interface Design Enable Stable Li-Rich Cathode, *J. Am. Chem. Soc.*, 2020, **142**, 8918–8927.

9 H. Z. Porter, E. E. Foley, W. Jin, E. Chen, E. A. Lawrence, E. N. Bassey and R. J. Clément, Impact of Mg Substitution on the Structure, Stability, and Properties of the $Na_2Fe_2F_7$ Weberite Cathode, *ACS Mater. Au*, 2024, **5**, 170–181.

10 L. Zhu, L. Li, J. Wen and Y. R. Zeng, Structural Stability and Ionic Transport Property of $NaMPO_4$ (M = V, Cr, Mn, Fe, Co, Ni) as Cathode Material for Na-Ion Batteries, *J. Power Sources*, 2019, **438**, 227016.

11 C. Daniel, D. Mohanty, J. Li and D. L. Wood, Cathode Materials Review, *AIP Conf. Proc.*, 2014, **1597**, 26–43.

12 J. Zheng, J. Xiao, X. Yu, L. Kovarik, M. Gu, F. Omenya, X. Chen, X. Q. Yang, J. Liu, G. L. Graff, M. S. Whittingham and J. G. Zhang, Enhanced Li + Ion Transport in $LiNi_{0.5}Mn_{1.5}O_4$ through Control of Site Disorder, *Phys. Chem. Chem. Phys.*, 2012, **14**, 13515–13521.

13 H. Liu, Q. Cao, L. J. Fu, C. Li, Y. P. Wu and H. Q. Wu, Doping Effects of Zinc on $LiFePO_4$ Cathode Material for Lithium Ion Batteries, *Electrochem. Commun.*, 2006, **8**, 1553–1557.

14 J. W. Fergus, Recent Developments in Cathode Materials for Lithium Ion Batteries, *J. Power Sources*, 2010, **195**, 939–954.

15 J. B. Goodenough, Metallic Oxides, *Prog. Solid State Chem.*, 1971, **5**, 145–399.

16 O. M. Karakulina, N. R. Khasanova, O. A. Drozhzhin, A. A. Tsirlin, J. Hadermann, E. V. Antipov and A. M. Abakumov, Antisite Disorder and Bond Valence Compensation in Li_2FePO_4F Cathode for Li-Ion Batteries, *Chem. Mater.*, 2016, **28**, 7578–7581.

17 Y. Liu, X. Rong, R. Bai, R. Xiao, C. Xu, C. Zhang, J. Xu, W. Yin, Q. Zhang, X. Liang, Y. Lu, J. Zhao, L. Chen and Y. S. Hu, Identifying the Intrinsic Anti-Site Defect in Manganese-Rich NASICON-Type Cathodes, *Nat. Energy*, 2023, (8), 1088–1096.

18 T. Mori, T. Masese, Y. Orikasa, Z. D. Huang, T. Okado, J. Kim and Y. Uchimoto, Anti-Site Mixing Governs the Electrochemical Performances of Olivine-Type $MgMnSiO_4$ Cathodes for Rechargeable Magnesium Batteries, *Phys. Chem. Chem. Phys.*, 2016, **18**, 13524–13529.

19 G. R. Gardiner and M. S. Islam, Anti-Site Defects and Ion Migration in the $LiFe_{0.5}Mn_{0.5}PO_4$ Mixed-Metal Cathode Material, *Chem. Mater.*, 2010, **22**, 1242–1248.

20 H. Chen, J. A. Dawson and J. H. Harding, Effects of Cationic Substitution on Structural Defects in Layered Cathode Materials $LiNiO_2$, *J. Mater. Chem. A*, 2014, **2**, 7988–7996.

21 R. Shunmugasundaram, R. S. Arumugam and J. R. Dahn, A Study of Stacking Faults and Superlattice Ordering in Some Li-Rich Layered Transition Metal Oxide Positive Electrode Materials, *J. Electrochem. Soc.*, 2016, **163**, A1394–A1400.

22 D. Eum, S. O. Park, H. Y. Jang, Y. Jeon, J. H. Song, S. Han, K. Kim and K. Kang, Electrochemomechanical Failure in Layered Oxide Cathodes Caused by Rotational Stacking Faults, *Nat. Mater.*, 2024, **238**(23), 1093–1099.

23 M. Han, Z. Liu, X. Shen, L. Yang, X. Shen, Q. Zhang, X. Liu, J. Wang, H.-J. Lin, C.-T. Chen, C.-W. Pao, J.-L. Chen, Q. Kong, X. Yu, R. Yu, L. Gu, Z. Hu, X. Wang, Z. Wang, L. Chen, M. Han, Z. Liu, L. Yang, J. Wang, X. Yu, Z. Wang, L. Chen, X. Shen, R. Yu, L. Gu, X. Wang, Q. Zhang, X. Liu, -J. H. Lin, C.-T. Chen, C.-W. Pao, J.-L. Chen, Q. Kong and Z. Hu, Stacking Faults Hinder Lithium Insertion in Li_2RuO_3, *Adv. Energy Mater.*, 2020, **10**, 2002631.

24 J. M. Kim and H. T. Chung, Electrochemical Characteristics of Orthorhombic $LiMnO_2$ with Different Degrees of Stacking Faults, *J. Power Sources*, 2003, **115**, 125–130.

25 W. Zeng, W. Shu, J. Zhu, F. Xia, J. Wang, W. Tian, J. Tian, S. Zhang, Y. Zhang, H. Peng, H. Zhao, L. Chen, J. Wu and S. Mu, Stacking Fault Slows Down Ionic Transport Kinetics in Lithium-Rich Layered Oxides, *ACS Energy Lett.*, 2024, **9**, 346–354.

26 Z. Lu, Z. Chen and J. R. Dahn, Lack of Cation Clustering in Li $[Ni_xLi_{1/3-2x/3}Mn_{2/3-x/3}]O_2$ ($0 < x \leq 1/2$) and $Li[Cr XLi_{(1-x)/3}Mn_{(2-2x)/3}]O_2$ ($0 < x < 1$), *Chem. Mater.*, 2003, **15**, 3214–3220.

27 R. Lin, E. Hu, M. Liu, Y. Wang, H. Cheng, J. Wu, J. C. Zheng, Q. Wu, S. Bak, X. Tong, R. Zhang, W. Yang, K. A. Persson, X. Yu, X. Q. Yang and H. L. Xin, Anomalous Metal Segregation in Lithium-Rich Material Provides Design Rules for Stable Cathode in Lithium-Ion Battery, *Nat. Commun.*, 2019, (10), 1–11.

28 L. Mu, R. Zhang, W. H. Kan, Y. Zhang, L. Li, C. Kuai, B. Zydlewski, M. M. Rahman, C. J. Sun, S. Sainio, M. Avdeev, D. Nordlund, H. L. Xin and F. Lin, Dopant Distribution in Co-Free High-Energy Layered Cathode Materials, *Chem. Mater.*, 2019, **31**, 9769–9776.

29 C. Liu, Z. Cui and A. Manthiram, Tuning Dopant Distribution for Stabilizing the Surface of High-Nickel Layered Oxide Cathodes for Lithium-Ion Batteries, *Adv. Energy Mater.*, 2024, **14**, 2302722.

30 R. J. Clément, Z. Lun and G. Ceder, Cation-Disordered Rocksalt Transition Metal Oxides and Oxyfluorides for High Energy Lithium-Ion Cathodes, *Energy Environ. Sci.*, 2020, **13**, 345–373.

31 H. Zhang, X. Gao, Q. Cai, X. Zhang, Y. Tian, M. Jia, W. Xie, Y. Du and X. Yan, Recent Progress and Perspectives on Cation Disordered Rock-Salt Material for Advanced Li-Ion Batteries, *J. Mater. Chem. A*, 2023, **11**, 8426–8452.

32 D. Chen, J. Ahn and G. Chen, An Overview of Cation-Disordered Lithium-Excess Rocksalt Cathodes, *ACS Energy Lett.*, 2021, **6**, 1358–1376.

33 H. Liu, Z. Zhu, Q. Yan, S. Yu, X. He, Y. Chen, R. Zhang, L. Ma, T. Liu, M. Li, R. Lin, Y. Chen, Y. Li, X. Xing, Y. Choi, L. Gao,

H. S. yun Cho, K. An, J. Feng, R. Kostecki, K. Amine, T. Wu, J. Lu, H. L. Xin, S. P. Ong and P. Liu, A Disordered Rock Salt Anode for Fast-Charging Lithium-Ion Batteries, *Nature*, 2020, **585**, 63–67.

34 H. Lin, W. T. Peng, Z. Wang, J. Hofmann, S. M. Vornholt, H. Liu, S. Wang, J. Holoubek, K. Zhou, Q. Miao, S. Huber, K. W. Chapman, S. P. Ong and P. Liu, Increasing the Energy Density of Disordered Rock Salt Anodes for Fast-Charging Lithium-Ion Batteries, *ACS Mater. Lett.*, 2025, **18**, 699–706.

35 Y. He, Z. He and B. Ouyang, Design Principle of Disordered Rocksalt Type Overlithiated Anode for High Energy Density Batteries, *Mater. Horizons*, 2024, **11**, 6049–6056.

36 D. Andre, S. J. Kim, P. Lamp, S. F. Lux, F. Maglia, O. Paschos and B. Stiaszny, Future Generations of Cathode Materials: An Automotive Industry Perspective, *J. Mater. Chem. A*, 2015, **3**, 6709–6732.

37 Y. Xia, J. Zheng, C. Wang and M. Gu, Designing Principle for Ni-Rich Cathode Materials with High Energy Density for Practical Applications, *Nano Energy*, 2018, **49**, 434–452.

38 K. M. Colbow, J. R. Dahn and R. R. Haering, Structure and Electrochemistry of the Spinel Oxides $LiTi_2O_4$ and $Li_{43}Ti_{53}O_4$, *J. Power Sources*, 1989, **26**, 397–402.

39 T. F. Yi, S. Y. Yang and Y. Xie, Recent Advances of $Li_4Ti_5O_{12}$ as a Promising next Generation Anode Material for High Power Lithium-Ion Batteries, *J. Mater. Chem. A*, 2015, **3**, 5750–5777.

40 T. F. Yi, L. J. Jiang, J. Shu, C. B. Yue, R. S. Zhu and H. B. Qiao, Recent Development and Application of $Li_4Ti_5O_{12}$ as Anode Material of Lithium Ion Battery, *J. Phys. Chem. Solids*, 2010, **71**, 1236–1242.

41 H. Zhang, Y. Yang, H. Xu, L. Wang, X. Lu and X. He, $Li_4Ti_5O_{12}$ Spinel Anode: Fundamentals and Advances in Rechargeable Batteries, *InfoMat*, 2022, **4**, e12228.

42 J. Lee, A. Urban, X. Li, D. Su, G. Hautier and G. Ceder, Unlocking the Potential of Cation-Disordered Oxides for Rechargeable Lithium Batteries, *Science*, 2014, **343**, 519–522.

43 Y. Sun, S. Jiao, J. Wang, Y. Zhang, J. Liu, X. Wang, L. Kang, X. Yu, H. Li, L. Chen and X. Huang, Expandable Li Percolation Network: The Effects of Site Distortion in Cation-Disordered Rock-Salt Cathode Material, *J. Am. Chem. Soc.*, 2023, **145**, 11717–11726.

44 L. Li, B. Ouyang, Z. Lun, H. Huo, D. Chen, Y. Yue, C. Ophus, W. Tong, G. Chen, G. Ceder and C. Wang, Atomic-Scale Probing of Short-Range Order and Its Impact on Electrochemical Properties in Cation-Disordered Oxide Cathodes, *Nat. Commun.*, 2023, **141**(14), 1–9.

45 A. Urban, J. Lee and G. Ceder, The Configurational Space of Rocksalt-Type Oxides for High-Capacity Lithium Battery Electrodes, *Adv. Energy Mater.*, 2014, **4**, 1400478.

46 H. M. Hau, T. Holstun, E. Lee, B. L. D. Rinkel, T. P. Mishra, M. Markuson DiPrince, R. S. Mohanakrishnan, E. C. Self, K. A. Persson, B. D. McCloskey and G. Ceder, Disordered Rocksalts as High-Energy and Earth-Abundant Li-Ion Cathodes, *Adv. Mater.*, 2025, 2502766.

47 M. Wang, X. Chen, H. Yao, G. Lin, J. Lee, Y. Chen and Q. Chen, Research Progress in Lithium-Excess Disordered Rock-Salt Oxides Cathode, *Energy Environ. Mater.*, 2022, **5**, 1139–1154.

48 H. Ji, A. Urban, D. A. Kitchaev, D.-H. Kwon, N. Artrith, C. Ophus, W. Huang, Z. Cai, T. Shi, J. C. Kim, H. Kim and G. Ceder, Hidden Structural and Chemical Order Controls Lithium Transport in Cation-Disordered Oxides for Rechargeable Batteries, *Nat. Commun.*, 2019, **10**, 592.

49 M. A. Jones, P. J. Reeves, I. D. Seymour, M. J. Cliffe, S. E. Dutton and C. P. Grey, Short-Range Ordering in a Battery Electrode, the 'Cation-Disordered' Rocksalt $Li_{1.25}Nb_{0.25}Mn_{0.5}O_2$, *Chem. Commun.*, 2019, **55**, 9027–9030.

50 Z. Cai, Y. Zhang, Z. Lun, B. Ouyang, L. C. Gallington, Y. Sun, H. Hau, Y. Chen, M. C. Scott and G. Ceder, Thermodynamically Driven Synthetic Optimization for Cation-Disordered Rock Salt Cathodes, *Adv. Energy Mater.*, 2022, **12**, 2103923.

51 B. Ouyang, N. Artrith, Z. Lun, Z. Jadidi, D. A. Kitchaev, H. Ji, A. Urban and G. Ceder, Effect of Fluorination on Lithium Transport and Short-Range Order in Disordered-Rocksalt-Type Lithium-Ion Battery Cathodes, *Adv. Energy Mater.*, 2020, **10**, 1903240.

52 Y. Shirazi Moghadam, S. Dinda, A. El Kharbachi, G. Melinte, C. Kübel and M. Fichtner, Structural and Electrochemical Insights from the Fluorination of Disordered Mn-Based Rock Salt Cathode Materials, *Chem. Mater.*, 2022, **34**, 2268–2281.

53 W. D. Richards, S. T. Dacek, D. A. Kitchaev, G. Ceder, O. Li, W. D. Richards, S. T. Dacek, D. A. Kitchaev and G. Ceder, Fluorination of Lithium-Excess Transition Metal Oxide Cathode Materials, *Adv. Energy Mater.*, 2018, **8**, 1701533.

54 Z. Cai, B. Ouyang, H. M. Hau, T. Chen, R. Giovine, K. P. Koirala, L. Li, H. Ji, Y. Ha, Y. Sun, J. Huang, Y. Chen, V. Wu, W. Yang, C. Wang, R. J. Clément, Z. Lun and G. Ceder, In Situ Formed Partially Disordered Phases as Earth-Abundant Mn-Rich Cathode Materials, *Nat. Energy*, 2024, **9**, 27–36.

55 T. Li, T. S. Geraci, K. P. Koirala, A. Zohar, E. N. Bassey, P. A. Chater, C. Wang, A. Navrotsky and R. J. Clément, Structural Evolution in Disordered Rock Salt Cathodes, *J. Am. Chem. Soc.*, 2024, **146**, 24296–24309.

56 K. Zhou, Y. Li, S. Zheng, M. Zhang, C. Zhang, C. Battaglia, H. Liu, K. Wang, P. Yan, J. Liu and Y. Yang, Tailoring the Redox-Active Transition Metal Content to Enhance Cycling Stability in Cation-Disordered Rock-Salt Oxides, *Energy Storage Mater.*, 2021, **43**, 275–283.

57 H. M. Hau, T. Mishra, C. Ophus, T. Y. Huang, K. Bustilo, Y. Sun, X. Yang, T. Holstun, X. Zhao, S. Wang, Y. Ha, G. H. Lee, C. Song, J. Turner, J. Bai, L. Ma, K. Chen, F. Wang, W. Yang, B. D. McCloskey, Z. Cai and G. Ceder, Earth-Abundant Li-Ion Cathode Materials with Nanoengineered Microstructures, *Nat. Nanotechnol.*, 2024, **19**, 1831–1839.

58 J. D. Langhout, E. Gager, T. Ulloa, S. Shepard, J. C. Nino and M. M. Butala, Isovalent Substitution Modulates Average and Short-Range Structure in Disordered Rocksalt Oxides, *J. Mater. Chem. A*, 2024, **12**, 32140–32153.

59 H. Li, R. Fong, M. Woo, H. Ahmed, D. H. Seo, R. Malik and J. Lee, Toward High-Energy Mn-Based Disordered-Rocksalt Li-Ion Cathodes, *Joule*, 2022, **6**, 53–91.

60 N. Yabuuchi, M. Takeuchi, M. Nakayama, H. Shiiba, M. Ogawa, K. Nakayama, T. Ohta, D. Endo, T. Ozaki, T. Inamasu, K. Sato and S. Komaba, High-Capacity Electrode Materials for Rechargeable Lithium Batteries: Li_3NbO_4-Based System with Cation-Disordered Rocksalt Structure, *Proc. Natl. Acad. Sci. U. S. A.*, 2015, **112**, 7650–7655.

61 Y. Kobayashi, M. Sawamura, S. Kondo, M. Harada, Y. Noda, M. Nakayama, S. Kobayakawa, W. Zhao, A. Nakao, A. Yasui, H. B. Rajendra, K. Yamanaka, T. Ohta and N. Yabuuchi, Activation and Stabilization Mechanisms of Anionic Redox for Li Storage Applications: Joint Experimental and Theoretical Study on Li_2TiO_3–$LiMnO_2$ Binary System, *Mater. Today*, 2020, **37**, 43–55.

62 J. Ahn, Y. Ha, R. Satish, R. Giovine, L. Li, J. Liu, C. Wang, R. J. Clement, R. Kostecki, W. Yang and G. Chen, Exceptional Cycling Performance Enabled by Local Structural Rearrangements in Disordered Rocksalt Cathodes, *Adv. Energy Mater.*, 2022, **12**, 2200426.

63 Y. Wang, W. Choe, Y. Ding, R. Liu, D. Nordlund and D. Chen, Advancing Mn-Based Li-Ion Battery Cathodes *via* a Partially Cation-Disordered Zigzag-Type Li–Nb–Mn–O Framework, *J. Am. Chem. Soc.*, 2025, **147**, 13437–13446.

64 W. H. Kan, C. Wei, D. Chen, T. Bo, B. Wang, Y. Zhang, Y. Tian, J. Lee, Y. Liu and G. Chen, Evolution of Local Structural Ordering and Chemical Distribution upon Delithiation of a Rock Salt–Structured $Li_{1.3}Ta_{0.3}Mn_{0.4}O_2$ Cathode, *Adv. Funct. Mater.*, 2019, **29**, 1808294.

65 M. Odetallah and C. Kuss, A Review of Chemically Induced Intercalation and Deintercalation in Battery Materials, *Energy Technol.*, 2023, **11**, 2201060.

66 C. Tian, Y. Xu, D. Nordlund, F. Lin, J. Liu, Z. Sun, Y. Liu and M. Doeff, Charge Heterogeneity and Surface Chemistry in Polycrystalline Cathode Materials, *Joule*, 2018, **2**, 464–477.

67 N. Nitta, F. Wu, J. T. Lee and G. Yushin, Li-Ion Battery Materials: Present and Future, *Mater. Today*, 2015, **18**, 252–264.

68 J. Choa and M. M. Thackeray, Structural Changes of $LiMn_2O_4$ Spinel Electrodes during Electrochemical Cycling, *J. Electrochem. Soc.*, 1999, **146**, 3577–3581.

69 M. M. M. Thackeray, P. J. J. Johnson, L. A. A. de Picciotto, P. G. G. Bruce and J. B. B. Goodenough, Electrochemical Extraction of Lithium from $LiMn_2O_4$, *Mater. Res. Bull.*, 1984, **19**, 179–187.

70 J. J. Rehr and R. C. Albers, Theoretical Approaches to X-Ray Absorption Fine Structure, *Rev. Mod. Phys.*, 2000, **72**, 621.

71 T. Yamamoto, Assignment of Pre-Edge Peaks in K-Edge X-Ray Absorption Spectra of 3d Transition Metal Compounds: Electric Dipole or Quadrupole?, *X-Ray Spectrom.*, 2008, **37**, 572–584.

72 F. Farges, *Ab Initio* and Experimental Pre-Edge Investigations of the Mn K-Edge XANES in Oxide-Type Materials, *Phys. Rev. B: Condens. Matter Mater. Phys.*, 2005, **71**, 155109.

73 S. R. Wasserman, P. G. Allen, K. Shuh, J. J. Bucher and N. M. Edelstein, EXAFS and Principal Component Analysis: A New Shell Game, *J. Synchrotron Radiat.*, 1999, **6**, 284–286.

74 J. Ahn, R. Giovine, V. C. Wu, K. P. Koirala, C. Wang, R. J. Clément and G. Chen, Ultrahigh-Capacity Rocksalt Cathodes Enabled by Cycling-Activated Structural Changes, *Adv. Energy Mater.*, 2023, **13**, 2300221.

75 J. Hornstra, Dislocations, Stacking Faults and Twins in the Spinel Structure, *J. Phys. Chem. Solids*, 1960, **15**, 311–323.

76 S. Anand, T. P. Mishra, P. Zhong, Y. Choi, K. J. Jun, T. Holstun and G. Ceder, Origin of Enhanced Performance When Mn-Rich Rocksalt Cathodes Transform to δ-DRX, *Mater. Today*, 2025, **88**, 210–218.

77 T. Holstun, T. P. Mishra, L. Huang, H. M. Hau, S. Anand, X. Yang, C. Ophus, K. Bustillo, L. ma, S. Ehrlich and G. Ceder, Accelerating the Electrochemical Formation of the δ Phase in Manganese-Rich Rocksalt Cathodes, *Adv. Mater.*, 2025, **37**, 2412871.

78 Y. J. Lee, F. Wang and C. P. Grey, 6Li and 7Li MAS NMR Studies of Lithium Manganate Cathode Materials, *J. Am. Chem. Soc.*, 1998, **120**, 12601–12613.

79 R. Pigliapochi, I. D. Seymour, C. Merlet, A. J. Pell, D. T. Murphy, S. Schmid and C. P. Grey, Structural Characterization of the Li-Ion Battery Cathode Materials $LiTi_xMn_{2-x}O_4$ ($0.2 \leq x \leq 1.5$): A Combined Experimental 7Li NMR and First-Principles Study, *Chem. Mater.*, 2018, **30**, 817–829.

80 Y. J. Lee, F. Wang, S. Mukerjee, J. McBreen and C. P. Grey, 6Li and 7Li Magic-Angle Spinning Nuclear Magnetic Resonance and *In Situ* X-Ray Diffraction Studies of the Charging and Discharging of $Li_xMn_2O_4$ at 4 V, *J. Electrochem. Soc.*, 2000, **147**, 803.

81 Y. Joo Lee and C. P. Grey, 6Li Magic-Angle Spinning (MAS) NMR Study of Electron Correlations, Magnetic Ordering, and Stability of Lithium Manganese(III) Oxide, *Chem. Mater.*, 2000, **12**, 3871–3878.

82 M. M. Thackeray, Manganese Oxides for Lithium Batteries, *Prog. Solid State Chem.*, 1997, **25**, 1–71.

83 A. Van Der Ven, C. Marianetti, D. Morgan and G. Ceder, Phase Transformations and Volume Changes in Spinel $Li_xMn_2O_4$, *Solid State Ionics*, 2000, **135**, 21–32.

84 E. Lee, D. H. Lee, S. Bessette, S. W. Park, N. Brodusch, G. Lazaris, H. Kim, R. Malik, R. Gauvin, D. H. Seo and J. Lee, Nearly All-Active-Material Cathodes Free of Nickel and Cobalt for Li-Ion Batteries, *Energy Environ. Sci.*, 2024, **17**, 3753–3764.

85 M. Scharrer, L. Bonatti, T. Geraci, S. V. Ushakov, J. Majzlan, M. Bustamante, H. Kojitani, X. Guo, H. Xu, L. Zhang, K. Lilova, S. Hayun, T. Subramani and A. Navrotsky, The Joys and Jitters of High-Temperature Calorimetry, *J. Am. Ceram. Soc.*, 2025, **108**, e20381.

86 A. K. Cheetham, V. E. F. Fender and R. I. Taylor, High Temperature Neutron Diffraction Study of Fe1-XO, *J. Phys. C: Solid State Phys.*, 1971, **4**, 2160–2165.

87 V. C. Wu, E. A. Lawrence, T. Li, E. N. Bassey, C. Y. Chang, B. J. Hwang, P. E. Cabelguen and R. J. Clément, High

Energy Density and Micrometer-Sized D0-Free Disordered Rocksalt Cathodes, *Energy Environ. Sci.*, 2025, **18**, 8918–8928.

88 J. Bhattacharya and A. Van Der Ven, Phase Stability and Nondilute Li Diffusion in Spinel $Li_{1+x}Ti_2O_4$, *Phys. Rev. B: Condens. Matter Mater. Phys.*, 2010, **81**, 104304.

89 A. Van Der Ven, J. Bhattacharya and A. A. Belak, Understanding Li Diffusion in Li-Intercalation Compounds, *Acc. Chem. Res.*, 2013, **46**, 1216–1225.

90 B. Xu and S. Meng, Factors Affecting Li Mobility in Spinel $LiMn_2O_4$—A First-Principles Study by GGA and GGA + U Methods, *J. Power Sources*, 2010, **195**, 4971–4976.